ARTICLE

Germline *PTEN* genotype-dependent phenotypic divergence during the early neural developmental process of forebrain organoids

Shin Chung Kang[1,7], Nicholas B. Sarn[1,7], Juan Venegas[1,7], Zhibing Tan[1,2], Masahiro Hitomi[1,2] and Charis Eng[1,2,3,4,5,6]✉

PTEN germline mutations account for ~0.2–1% of all autism spectrum disorder (ASD) cases, as well as ~17% of ASD patients with macrocephaly, making it one of the top ASD-associated risk genes. Individuals with germline *PTEN* mutations receive the molecular diagnosis of *PTEN* Hamartoma Tumor Syndrome (PHTS), an inherited cancer predisposition syndrome, about 20–23% of whom are diagnosed with ASD. We generated forebrain organoid cultures from gene-edited isogenic human induced pluripotent stem cells (hiPSCs) harboring a $PTEN^{G132D}$ (ASD) or $PTEN^{M134R}$ (cancer) mutant allele to model how these mutations interrupt neurodevelopmental processes. Here, we show that the $PTEN^{G132D}$ allele disrupts early neuroectoderm formation during the first several days of organoid generation, and results in deficient electrophysiology. While organoids generated from $PTEN^{M134R}$ hiPSCs remained morphologically similar to wild-type organoids during this early stage in development, we observed disrupted neuronal differentiation, radial glia positioning, and cortical layering in both *PTEN*-mutant organoids at the later stage of 72+ days of development. Perifosine, an AKT inhibitor, reduced over-activated AKT and partially corrected the abnormalities in cellular organization observed in $PTEN^{G132D}$ organoids. Single cell RNAseq analyses on early-stage organoids revealed that genes related to neural cell fate were decreased in $PTEN^{G132D}$ mutant organoids, and AKT inhibition was capable of upregulating gene signatures related to neuronal cell fate and CNS maturation pathways. These findings demonstrate that different *PTEN* missense mutations can have a profound impact on neurodevelopment at diverse stages which in turn may predispose PHTS individuals to ASD. Further study will shed light on ways to mitigate pathological impact of *PTEN* mutants on neurodevelopment by stage-specific manipulation of downstream PTEN signaling components.

Molecular Psychiatry (2024) 29:1767–1781; https://doi.org/10.1038/s41380-023-02325-3

INTRODUCTION

Autism spectrum disorder (ASD) is characterized by deficits in social communication, accompanied by restricted repetitive behaviors and interests [1]. ASD represents a significant clinical and scientific challenge due to the complex gene-environment interactions which give rise to the disorder, as well as high prevalence affecting 1:44 children in the United states and Canada [1–7]. Post-mortem characterization of ASD patient brains has revealed several common cellular pathologies consistent among those with ASD. These include reactive astrocytosis, alterations in myelination, activated microglia, reduction in neuron density, disorganized cortical layering, and macro- or microcephaly [8–10]. It is thought that these pathological changes to the central nervous system (CNS) represents only a handful of the underlying pathological contributions to ASD, reflecting the need for more mechanistic studies focused on a cellular level in order to understand the pathogenesis of the disorder. Fortunately, as technology advances and new in vitro techniques are developed to model the early phases of brain development and cellular function, we move closer to identifying and understanding the molecular mechanisms that contribute to the disorder.

Individuals with a germline *PTEN* mutation have the molecular diagnosis of *PTEN* Hamartoma Tumor Syndrome (PHTS), an inherited cancer predisposition syndrome, about 20–23% of whom are diagnosed with ASD [11]. Moreover, we and others have demonstrated that germline *PTEN* mutations occur in ~7–17% of ASD patients with macrocephaly [7, 11–15]. This makes *PTEN* one of the top-ranking syndromic ASD risk genes annotated by the Simons Foundation Autism Research Initiative (SFARI), and *PTEN* mutations are estimated to account for ~0.2–1% of all reported ASD cases, making it an excellent candidate gene for study to elucidate the underlying cellular mechanisms contributing to ASD [16–18].

Recently, organoids from human induced pluripotent stem cells (hiPSCs) have served as an excellent in vitro model system to study complex biological processes. Forebrain (FB) organoid model systems have been used to model neural tube formation, neuronal

[1]Genomic Medicine Institute, Lerner Research Institute, Cleveland Clinic, Cleveland, OH 44195, USA. [2]Cleveland Clinic Lerner College of Medicine, Case Western Reserve University, Cleveland, OH 44195, USA. [3]Center for Personalized Genetic Healthcare, Medical Specialties Institute, Cleveland Clinic, Cleveland, OH 44195, USA. [4]Case Comprehensive Cancer Center, Case Western Reserve University School of Medicine, Cleveland, OH 44106, USA. [5]Taussig Cancer Institute, Cleveland Clinic Foundation, Cleveland, OH 44195, USA. [6]Department of Genetics and Genome Sciences, Case Western Reserve University School of Medicine, Cleveland, OH 44106, USA. [7]These authors contributed equally: Shin Chung Kang, Nicholas B. Sarn, Juan Venegas. ✉email: engc@ccf.org

Received: 6 April 2023 Revised: 22 October 2023 Accepted: 13 November 2023
Published online: 29 November 2023

maturation, and cortical layering, making them an exceptional model to help study early human brain development in the context of neurodevelopmental disorders such as ASD [19–33]. Since the lipid phosphatase activity of PTEN regulates cellular polarity and migration of immature neurons by antagonizing the phosphatidylinositol 3 kinase (PI3K)-AKT signaling pathway, we utilized FB organoid cultures derived from *PTEN* gene-edited hiPSCs to investigate how early brain development is affected by different germline *PTEN* mutations [34–36]. We selected two *PTEN* missense mutations identified in our PHTS patient cohort. These are $PTEN^{M134R}$ which has been found in PHTS patients without ASD (PHTS-cancer), and $PTEN^{G132D}$ which is observed in PHTS patients with ASD (PHTS-ASD). Characterization of FB organoids derived from genetically modified hiPSCs found in PHTS and ASD patient cohorts provide valuable information into the underlying cellular mechanisms contributing to ASDs.

Here, we show that the $PTEN^{G132D}$ mutant allele associated with PHTS-ASD disrupts early neuroectoderm and electrophysiological function during the first several days of FB organoid generation, while organoids generated from the $PTEN^{M134R}$ PHTS-cancer remain morphologically similar to $PTEN^{WT/WT}$. However, we did observe disrupted neuronal differentiation and cortical layering in both mutant FB organoids at the mature stage of 72+ days. Finally, disrupted neuroectoderm formation in the $PTEN^{G132D/WT}$ organoid culture was partially rescued by pharmacological AKT inhibition via Perifosine during the early forebrain induction between days 0 and 7. We also observed that Perifosine treatment helped to rescue neural tube formation resulting in more circular lumens with correctly oriented radial glial cell (RGC) progenitors during early forebrain induction in $PTEN^{G132D/WT}$ organoids, which was accompanied by the shift in transcriptomic signature suggestive of neuroectodermal differentiation. These results demonstrate two divergent cellular and organismal phenotypes in early neural development that are dependent solely on the genotype of *PTEN*, with the most severe pathogenesis arising from clinically relevant PHTS-ASD mutation. Furthermore, these data indicate there may be universally relevant underlying cellular mechanisms contributing to PHTS-ASD, which in turn offer potentially targetable approaches *in utero* to ameliorate the severity or negate potential ASD in newborns harboring a germline *PTEN* mutation.

MATERIALS AND METHODS

Human induced pluripotent stem cell (hiPSC) culture

Two distinct PHTS patient-relevant *PTEN* mutations, PC640. PTEN. g4 132G > D and PC640. PTEN. g7 134M > R were engineered using CRISPR/Cas9 technology into a commercially available male skin fibroblast-derived hiPSC line (BJFF.6) by the Washington University Genome Engineering & Stem Cell Center, iPSC Core (GEiC, Washington University School of Medicine, St. Louis, MO 63108) [37]. Heterozygous mutation state was confirmed by next-generation sequencing (NGS) for clones of each *PTEN*-mutant. These established *PTEN-mutant* hiPSC lines and parental lines, which were maintained in supplemented StemFlex™ basal medium (ThermoFisher Scientific, Waltham, MA, cat. no. A3349301) in the plates that had been pre-coated with 1.6 µl/ml Geltrex™ LDEV-Free Reduced Growth Factor (Gibco™, ThermoFisher Scientific, cat. no. A1413202) in DMEM (Gibco™ DMEM, ThermoFisher Scientific, cat. no. 11995065) for overnight at 37 °C [37, 38].

Induction of forebrain organoids in 3-D culture

Forebrain (FB) organoids were generated from feeder-free hiPSCs using a previously reported protocol [31], with minor modifications, as follows. On day 0, embryoid bodies (EB) were generated with Collagenase IV and day 0 designates the day of induction of organoids from iPSCs. To create embryoid bodies, pre-warmed 1 ml of 1 mg/ml Collagenase type IV (MilliporeSigma, Burlington, MA, cat. no. 17104019) was added to the iPSC monolayer culture on day 0. After 45–90 min incubation at 37 °C and 5% CO_2, detached clusters of iPSCs were collected into 15 ml centrifuge tube with 5 ml serological pipette and sedimented by gravity. Supernatants were discarded and the settled clusters were washed with StemFlex™ basal Medium and re-suspended with the first FB induction medium (Table S1). Using a P1000 pipette with a cut tip having an orifice 3 mm or larger in diameter, the detached clusters were transferred to ultra-low attachment six-well plate (Corning Costar® ThermoFisher, cat. no. 3471) and incubated at 37 °C and 5% CO_2 for 24 h. Next, on day 1, we changed 3 ml FB induction medium, and on day 3 and 4, change half forebrain induction medium. On days 5 and 6, half of the medium from each well was removed and replaced with 1.5 ml of FB second medium (Table S1). On day 7, FB organoids were embedded with a 3:2 mixture of Geltrex™ and second medium. We used 100 µl of Geltrex™ and 67 µl of second medium to embed ~30 FB organoids and placed in 1 well of a non-treated 12 well cell culture plate (Costar®, ThermoFisher, cat. no. 3737). The embedded FB organoids were incubated for 30 min at 37 °C and 5% CO_2 to solidify the gel. Second medium was then added to each well and changed every other day until day 14. On day 14, induced FB organoids were removed from the gel and transferred to individual wells of a 12 well tissue culture plate equipped with a SpinΩ™ bioreactor (3Dnamics Inc., Baltimore, MD) spinning at a speed of 60 rpm. at 6 V [31]. FB organoids in the SpinΩ™ were maintained in the third FB medium (Table S1) until day 35. Starting at day 35, pre-thawed Matrigel was added into forebrain third medium at a dilution of 1:100 to create an extracellular matrix coating on the organoid surface. The FB organoids were maintained in the third medium with Matrigel up to days 72+. AKT was inhibited by adding the AKT inhibitor, 1 µM Perifosine (Cayman Chemical Company, Ann Arbor, MI, cat. no. 10008112) to cultures from day 0 to day 7 during the induction of FB organoids. We obtained a SpinΩ™ bioreactor and parts and assembled it as following the manufacturer's instruction (3Damics Inc., Baltimore, MD).

Immunostaining and imaging

Immunocytochemistry was performed as described in Kang et al. (2020) with minor modification, as follows [39]. FB organoids were fixed for 15 min at 4 °C with 4% paraformaldehyde diluted in phosphate buffered saline (PBS without Ca^{2+}, Mg^{2+}), pH of 7.4. Fixed organoids were washed with PBS three times and incubated overnight at 4 °C with 20% sucrose dissolved in PBS prior to embedding with Tissue -Tek O.C.T. Compound (Sakura Finetek USA, Inc. Torrance, CA, cat. no. 4583) or in Tissue-Tek Cryomold (Sakura Finetek USA, Inc. cat. no. 4565). Embedded organoids were cryo-sectioned at 12 µm using Cryostat (*Leica* Biosystems, Deer Park, IL, cat. no. *Leica* CM 1850 Cryostat), and affixed to polarized glass coverslips (ThermoFisher Scientific, Fisherbrand, cat. no. 12-550-15). Tissues were permeabilized for 15 min in 0.5% Triton X-100 dissolved in phosphate buffered saline (PBST) and then blocked with 5% normal goat serum (Vector Laboratories, Newark, CA, cat. no. S-1000) in PBST for 1 h at room temperature. After blocking, tissues were incubated overnight at 4 °C with primary antibodies in 5% normal goat serum in 0.5% Triton X-100 in PBS. After washing three times with PBS for 30 min at room temperature, tissues were incubated for 2 h at room temperature with secondary antibodies diluted in 0.3% Triton X-100 in PBS. Sections were then washed three times for 15 min each with PBS and then cover slips were mounted on slides with anti-fade mounting buffer containing 4′, 6-diamindino-2-phenylindole (DAPI) (Vector Laboratories, cat. no. H-1200). Images from immunostaining were acquired using the Leica TCS-SP8-AOBS inverted confocal microscope (*Leica* Microsystems, GmbH, Wetzlar, Germany, *Leica* SP8 confocal microscope). The total number of cells in each field was determined by counting DAPI positive cell nuclei. Differentiation and growth of neuroepithelia were quantified by measuring the area stained positive for the respective marker and normalized to the number of DAPI positive nuclei. Circular symmetry of the lumen in the corticogenesis units (circularity) were measured by outlining the lumen-stained positive cells for markers in using ImageJ (FIJI, GitHub, Version 2.0.0-rc-69/1.52n). At minimum $N = 3$ forebrain organoid batches were analyzed, and all experiments were repeated at least three independent times. For 3-dimensional organoid staining with the earlier stage (<7 days) of organoids, organoids were processed using the same procedure and imaged as whole organoids without cryosectioning.

Generation of neural progenitor cells (NPCs)

We induced neuroprogenitor cells from hiPSCs according to the previous report with slight modifications [31]. Briefly, with the same method, we created the EBs with collagenase IV and kept them in the growth medium in non-binding 6-well plate at 37 °C with 5% CO_2. After 24 h, conditions were switched to the NPC induction media 1 (Essential 6 medium, MEM-NEAA, GlutaMax, 100 ng/ml Noggin, 10 µM SB431542, 2-mercapthethanol) and the EBs were maintained for 7 days. On day 5, half induction media 2 (Neurobasal media, Invitrogen, cat. no. 21103-049: DMEM/F12 [1:1],

GlutaMax, 100 ng/ml Noggin (R&D systems, ca. no. 6057-NG), 10 µM SB431542, N2, B27 supplement) was added and on day 6, 100% media 2 was added into each well. On day 7, the EBs were transferred to Geltrex™ LDEV-Free Reduced Growth Factor-coated plate and maintained for the other 7 days. On day 14, the formed neural rosettes on the Geltrex™ LDEV-Free Reduced Growth Factor coated plates were detached by picking with a sterile tip and dissociated by pipetting. Dissociated NPCs were plated onto the Geltrex™ (LDEV-Free Reduced Growth Factor) coated 6-well plate and Geltrex-coated coverslip in 24-well plate and maintained with media 3 (Neurobasal™ Medium, Gibco™, cat. no. 21103049): DMEM/F12 [1:1] supplemented with GlutaMax, 20 ng/ml EGF (epidermal growth factor, R & D, cat. no. 236-EG-01M), and 10 ng/ml FGF2 (fibroblast growth factor 2, R & D, cat. no. 233-FB-500), (N2, B27) for 3 days. On day 17, EGF and FGF2 were depleted to initiate neural differentiation. 7, 14, 21, and 28 days after the growth factors' depletion, neuronal differentiation capability of the NPCs were confirmed by the expression of a neuronal marker, TUJ1, and sodium channel 1 alpha subunit, scn1A (NaV1.1) (ca. no. ASC-001, Alomone Labs, Israel).

Electrophysiology

Whole-cell patch clamp recordings from cultured NPCs were made using a phase-contrast microscope (Leica), a MultiClamp 700B amplifier, and a 1550B interface (Axon Instruments). Recording pipettes (3–6 MΩ tip resistance, B-150-86-10, Sutter Instruments) were filled with internal solution containing (mM): 125 K-gluconate, 15 KCl, 10 HEPES, 4 MgATP, 0.3 Na3GTP, 0.2 EGTA, 10 phosphocreatine (295 mOsm, pH 7.3, adjusted with KOH). The conventional extracellular solution contained (mM): 145 NaCl, 3 KCl, 2 MgCl2, 3 CaCl2, 10 HEPES, 10 D-glucose (300 mOsm, pH 7.3, adjusted with NaOH). For I_{Na} recording, the resting membrane potential was held −70 mV and membrane potential was changed from −90 mV to +40 mV at 10 mV per step. Meanwhile, I_{Na} was isolated by online P/N leak subtraction. Action potential recordings were made under current-clamp mode and step-current were injected from −25 pA to 200 pA at the step of 25 pA. Signals were filtered at 1 kHz using the amplifier circuitry, sampled at 10 kHz, and analyzed using Clampex 11 (Axon Instruments, USA).

Western blot analysis

Western blotting was performed as described [39]. Organoids were collected into microcentrifuge tubes by gravity sedimentation and washed three times with PBS, and ~20 organoids were lysed for 1 h on ice with M-PER™ (Mammalian Protein Extraction Reagent) buffer (ThermoFisher Scientific, cat. no. 78505) supplemented with phosphatase and protease inhibitor cocktails (MilliporeSigma, cat. no. P5726, P0044, P8340). Lysates were centrifuged at 4 °C for 15 min at 16,000 × *g*. Supernatants were collected, and protein concentration was determined by bicinchoninic acid (BCA) assay according to manufacturer's directions using BCA™ Protein Assay Kit (ThermoFisher Scientific, cat. no. 23228, 1859078). 15–20 µg of total protein lysates were separated on 4–20% polyacrylamide Criterion gels (Bio-Rad, Hercules, CA, cat. no. 64496731). The blots were blocked with 5% bovine serum albumin (BSA) in Tris-buffered saline, pH 7.4, with 0.025% Tween-20 (TBST), incubated for 1 h at room temperature prior to overnight primary antibody incubation at 4 °C. The next day, membranes were washed three times for 30 min with TBST. Next, horse radish peroxidase-conjugated secondary anti-mouse (Promega, Madison, WI, cat. no. PRW4021) or anti-rabbit antibodies (Promega, WI, cat. no. 4011) were added and incubation for 1 h at room temperature. Blots were imaged using an Amersham ImageQuant 600 CCD imager (Amersham™ Imager, GE HealthCare, Chicago, IL), to capture immunoreactive bands which were visualized by incubating with ECL chemiluminescence reagent Super-Signal™ West Pico PLUS Chemiluminescent Substrate (ThermoFisher Scientific, cat. no. 34578). All primary antibodies were diluted to 1:1000 and 1:2000 for secondary antibodies. Band intensity analysis was performed using ImageJ (software version 2.0.0-rc-69/1.52n).

Cell dissociation from organoids for single cell RNA sequencing

Twenty to thirty forebrain organoids induced with or without AKT inhibitor treatment for 7 days were transferred to a well of a 24-well plate and washed with PBS for three times. Organoids digestion was carried out using the TrypLE™ Select Enzyme (Gibco™, Thermofisher Scientific, cat. no. A1217701). 700 µl TrypLE™ Select Enzyme was added to each well and the samples were incubated with shaking (70 rpm) at 37 °C and 5% CO_2 for 15 min. 300 µl of cold 2% Bovine Serum Albumin (BSA) in PBS was added to each well to stop the digestion and the digested organoids were triturated by pipetting. The dissociated cells were transferred to the 15 ml conical tube, centrifuged at 900 rpm for 3 min at room temperature. After re-suspended in an appropriate volume of PBS, the cells were then passed through a 40 µm Corning© Cell Strainer (Corning, Thermofisher Scientific, cat. no. 431750). Cells were counted with trypan blue to note cell viability. The target concentration was 1000 cells/µl.

Sample processing with 10X genomics and cDNA library preparation

Using 10X Genomics Chromium Single Cell 3′ Reagents Kit (version 3.1), 6000 to 10,000 cells per sample were captured for library and sequencing generation. Following the organoid dissociation, the single cell suspension, the gel beads, and the emulsion oil was added to the 10X Genomics Single Cell Chip G. Immediately following the droplet generation, samples were transferred to a PCR 8-tube strip (USA scientific) for reverse transcription reaction using SimpliAmp thermal cycler (Applied Biosystems). cDNA generated by reverse transcription was recovered using the recovery reagent provided by 10X Genomics. The cDNA was cleaned up using the Silane DynaBeads according to the 10X Genomics user guide. The purified cDNA was amplified for 11 cycles and subsequently cleaned up using SPRIselect beads (Beckman Coulter). To determine the cDNA concentrations, 1:10 dilution of each sample was analyzed on an Agilent Bioanalyzer High Sensitivity chip. The cDNA libraries were constructed according to the Chromium Single Cell 3′ Reagent Kit version 3.1 user guide.

scRNAseq data analysis

The scRNAseq libraries were sequenced to a target depth of 50,000 read pairs per cell. De-multiplexed FASTQ files were processed using cellranger-4.0.0. Reads were mapped using the count pipeline. Reference genome refdata-gex-GRCh38-2020A and GTF from GENECODE v32 (GRCh28.p13) was used to align the reads. The filtering, normalization and downstream analysis was performed using Seurat 3.2.1 in R [40]. Briefly, the raw data was filtered for low-quality cells using the following QC thresholds. Cells with mitochondrial reads >10% of total mapped reads, gene counts <250 or gene features >40.000 where filtered, leaving 38,030 high-quality cells for the downstream analysis. Seurat's standard workflow was followed. Using the 2000 most variable genes, principal components (PCs) were computed, and the first 15 PCs were utilized to generate clustering at resolution 0.45 and UMAP was generated.

Monocle3 analysis

Because of the difficulty of performing an accurate cell calling in the SEURAT package, we performed a trajectory analysis using the standard workflow of Monocle3 [41–43]. The raw gene count per cell was log normalized and scaled before computing principal components (PCs). The UMAP coordinates from Seurat analysis were transferred to the monocle object to preserve the cluster identities across the two analysis sets. Monocle3 built a trajectory across the cells, based on gene expression changes that signify the different cell states transitions within the dataset. Next, cells across the trajectory were ordered based on user defined starting point (root) for the trajectory (CDH1, CDH2, POU5F1, NEUROD4, PAX6, MKI67, where used to establish the root in the UMAP topology). The lowest Pseudotime score was assigned to the root (cells with the highest *PU5F1*, *CDH1* expression, which are in cluster 2 and 3) while the remaining cells were assigned a score based on the tool's perception of subsequent order of the cell-state transitions. Genes that vary as a function of Pseudotime were deduced by running graph test function and plotted on Pseudotime scale.

Ingenuity pathway analysis

Differential expression analyses were conducted between previously filtered and normalized samples using loupe browser tool (10X Genomics) and Logfold2 parameters. All samples were examined against the whole data set transcriptomic background and against all other samples. Only high-count genes were taken into account as IPA input. Only those differentially expressed genes (DEGs) with log2fold changes >1 or <−1 and p-value < 0.05, were selected to for Ingenuity Pathway Analyses (IPA, QIAGEN) using the standard pipeline. Enrichment for diseases and functions was also examined using IPA.

Statistics

Data are expressed as the mean ± SD (standard deviation). Statistical significance was analyzed by one-way analysis of variance (ANOVA), followed

by post-hoc Tukey-Kramer analysis using Graph Pad Prism 8 program. We considered all *p*-values less than 0.05 to be statistically significant denoted in text, with statistical analysis found in the figure legends.

RESULTS

PTEN$^{WT/WT}$ forebrain organoids recapitulate neuroepithelial organization and cortical layering

We first generated *PTEN*$^{WT/WT}$ FB organoids using hiPSCs to confirm that our culture system is capable of recapitulating cellular organization similar to early forebrain formation. Using organoids generated from *PTEN*$^{WT/WT}$ hiPSCs, we observed that the embryoid bodies develop lumen-like structures between days 3 and 7 (Fig. 1a). On day 14, using Immunofluorescent (IF) staining, we observed forebrain-specific neural progenitor markers SOX2, PAX6, and NESTIN expressed in the deep cellular layers forming structures analogous to a neural tube within the forebrain organoid (Fig. 1b). These data indicate that neuroepithelium formation starts as early as day 7 and is proceeded by the formation of the neural tube-like structures we observed at day 14 (Fig. 1a, b). A fraction of these neural progenitor cells were positive for phospho-VIMENTIN (pVIM), a radial glial cell (RGC) marker (Fig. 1b). We observed pVIM^{+} cells located proximally to the organoid lumens with their spindle-shaped cell bodies projecting outward and perpendicularly to the luminal circumference, a morphological hallmark of typical RGCs [44]. We also observed KI67^{+} cells co-expressing SOX2 inside of the neural tube-like structure on day 14, indicating active cell proliferation in this region, and that these cells are analogous to neural stem cells that make up the subventricular zone (SVZ) of the developing cortex (Fig. 1b), where residing progenitor cells grow and contribute to apical and basal expansion of the early developing brain [45, 46]. These data indicate that forebrain organoids from hiPSCs recapitulate key developmental processes of early mammalian brain development.

To capture the later organizational and cellular features of forebrain development, we maintained forebrain organoids for 72 days in spinner culture. At this later stage of FB organoid induction, we observed well-defined ventricular zone (VZ)-like structures with highly packed SOX2^{+} neural progenitor cells (NPCs) near the lumen (Fig. 1c), similar to what we observed at 14 days in vitro (Fig. 1b). Outside of the NPC layer, we observed two additional layers consisting of distinctive populations of cells. These formed a subventricular zone (SVZ)-like structure comprising intermediate neurons expressing TBR1, and a cortical plate-like structure comprised of CTIP2^{+} (early-born cortical layer marker) and SATB2^{+} (late-born cortical layer marker) neurons (Fig. 1c). The arrangement and patterning of these two layers closely resemble those of the developing human cortex at gestational week 22 [25, 30]. All together, these observations indicate that forebrain organoid development in culture is very similar to human corticogenesis and proceeds developmental stages at a chronologically comparable pace. To avoid confusion, we will refer to these internal organoid structures comprising NPCs and RGCs on day 14 as "corticogenesis unit" from here forward (Fig. 2a).

PHTS-ASD *PTEN*^{G132D} allele impaired corticogenesis unit formation during early forebrain induction and neuronal electrophysiological maturation

FB organoids were induced from hiPSCs with two distinct *PTEN* mutations, an ASD-associated *PTEN*^{G132D} mutant allele, or a cancer-associated *PTEN*^{M134R} mutant allele to study how *PTEN* germline mutations impact the formation of corticogenesis units comprising neuroprogenitor cells positive for SOX2 and PAX6 found in the *PTEN*$^{WT/WT}$ control FB organoids (Fig. 2a). We utilized phase contrast imaging to examine forebrain organoid development at multiple stages (day 3, 5, 7, 14, 28, 35, and 72) to determine if morphological differences existed among *PTEN*$^{WT/WT}$, *PTEN*$^{G132D/WT}$ and *PTEN*$^{M134R/WT}$ forebrain organoids (Fig. 2b). In *PTEN*$^{WT/WT}$ and *PTEN*$^{M134R/WT}$ organoids a clearly defined lumen with an organized spherical morphology began to develop in the center of the organoid mass, which has a round and smooth translucent surface (Fig. 2b top and bottom at day 5). In contrast, the central lumens that formed in *PTEN*$^{G132D/WT}$ organoids had disfigured shapes with undefined boundaries on day 5, and their corticogenesis were less circular in shape compared to the other two genotypes (Fig. 2b). On day 7, corticogenesis units were translucently visible in *PTEN*$^{WT/WT}$ and *PTEN*$^{M134R/WT}$ organoids, and appeared indistinguishable from one another, while *PTEN*$^{G132D/WT}$ organoids had irregularly shaped corticogenesis units that appeared to be small and underdeveloped compared to *PTEN*$^{WT/WT}$ and *PTEN*$^{M134R/WT}$ organoids (Fig. 2b). The development of corticogenesis units in *PTEN*$^{M134R/WT}$ organoids were similar to that of *PTEN*$^{WT/WT}$ until day 28, when they became significantly larger in size, and showed overgrowth and folding of the outer layers comprising the organoids surface (Fig. 2b).

In addition to these data, we quantitatively analyzed organoid circularity from days 7 to 28 (Supplementary Fig. S1a), finding the greatest differences in circularity between *PTEN*$^{WT/WT}$, *PTEN*$^{G132D/WT}$ and *PTEN*$^{M134R/WT}$ forebrain organoids is between mid-development, days 8 and 14 (S1a), with *PTEN*$^{G132D/WT}$ being the most significantly decreased. Next, we quantified the diameter of all three organoid genotypes, and found there is an overall deficit in the mean organoid diameter by day 41 in the *PTEN*$^{G132D/WT}$ organoids (S1b). This size deficit remained until day 72 (S1b), while *PTEN*$^{WT/WT}$ and *PTEN*$^{M134R/WT}$ organoids remained roughly the same size during development, with *PTEN*$^{M134R/WT}$ being slightly larger than *PTEN*$^{WT/WT}$ by day 72 (S1b).

Moreover, to understand the developmental mechanisms contributing to the morphological differences among mutant organoids, we analyzed the neural progenitor organization unit at day 14 via immunofluorescence (IF) staining of SOX2 and PAX6 (Fig. 2c). We measured the overall perimeter of the corticogenesis unit indicated by the pattern of SOX2^{+} cells for all three organoid genotypes and found significantly decreased perimeter in *PTEN*$^{G132D/WT}$ organoids, p-value = 0.0001 and 0.005, respectively (Fig. 2c, d). Further examination also revealed that the corticogenesis units of *PTEN*$^{G132D/WT}$ organoids were extremely disorganized, and that the patterning of KI67^{+}, PAX6^{+}, and SOX2^{+} cells were sporadic compared to *PTEN*$^{WT/WT}$ and *PTEN*$^{M134R/WT}$ organoids (Fig. 2c). To characterize the cellular make-up of the corticogenesis units at day 14, we counted the number of neural progenitor cells (NPC) expressing SOX2 or PAX6 (Fig. 2e, f). The frequencies of NPCs expressing SOX2^{+} or PAX6^{+} normalized to the total nuclei per corticogenesis unit were highest in *PTEN*$^{WT/WT}$ organoids amongst the organoids of the three genotypes (Fig. 2e, f). While SOX2^{+} and PAX6^{+} cells in *PTEN*$^{M134R/WT}$ were lower than that of *PTEN*$^{WT/WT}$ (p-value = 0.045 and p-value < 0.0001 for respective markers), we found significantly low numbers of SOX2^{+} and PAX6^{+} cells in *PTEN*$^{G132D/WT}$ organoids having 58.57% lower in SOX2^{+} cells and 85.88% lower in PAX6^{+} cells than in *PTEN*$^{WT/WT}$ organoids, p-value < 0.0001 (Fig. 2e, f). Additionally, we examined mean expression of SOX2 and PAX6 at day 14 and found no significant differences in overall expression (S1c and S1d), suggesting the changes in cellular disorganization are not the result of decreased SOX2 and PAX6 in *PTEN*$^{G132D/WT}$ organoids. Overall, these data suggest that the ASD-associated mutant *PTEN*^{G132D} allele more severely disrupts NPC development, cellular organization and the expansion of NPC compared to the cancer-associated *PTEN*^{M134R}.

Neuronal maturation is most severely disrupted in ASD-associated *PTEN*$^{G132D/WT}$ organoids compared to non-ASD *PTEN*$^{M134R/WT}$ or *PTEN*$^{WT/WT}$ organoids

We next examined if the formation of distinctive cortical layers at the later phases of organoid development (day 28 and days 72+) was affected in *PTEN*$^{M134R/WT}$ and *PTEN*$^{G132D/WT}$ organoids. Forebrain organoids of all three genotypes harvested on days 28 and 72+

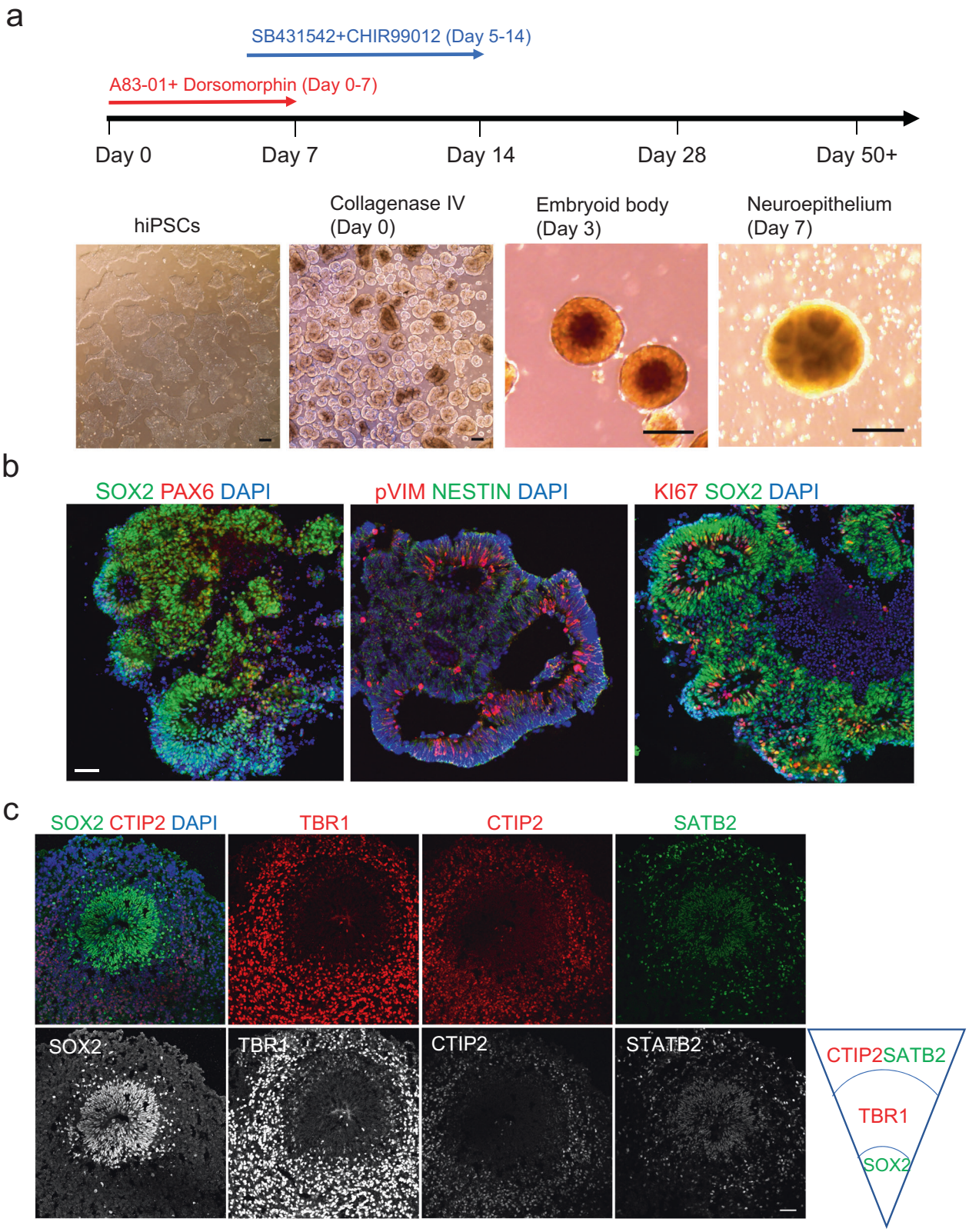

Fig. 1 Forebrain organoid culture recapitulates human brain development. a Schematic of forebrain organoid induction with representative phase contrasted images of various stages; hiPSCs, collagenase IV treated (Day 0), embryoid bodies (Day 3), and early forebrain organoid (Day 7). Scale bars indicate 200 µm. **b** IF staining of neural progenitor cell markers SOX2, PAX6, NESTIN, pVIM and KI67 (phosphorylated VIMENTIN) detected in *PTEN*$^{WT/WT}$ forebrain organoids induced from hiPSCs on day 14 of induction. Scale bar indicates 50 µm. **c** Representative IF staining of SOX2, TBR1, CTIP2, and, SATB2, in *PTEN*$^{WT/WT}$ forebrain organoids at day 72. Images shown are from consecutive sections for the same *PTEN*$^{WT/WT}$ corticogenesis unit. Scale bar indicates 50 µm. *<0.05, **<0.01, ***<0.001, ****<0.0001.

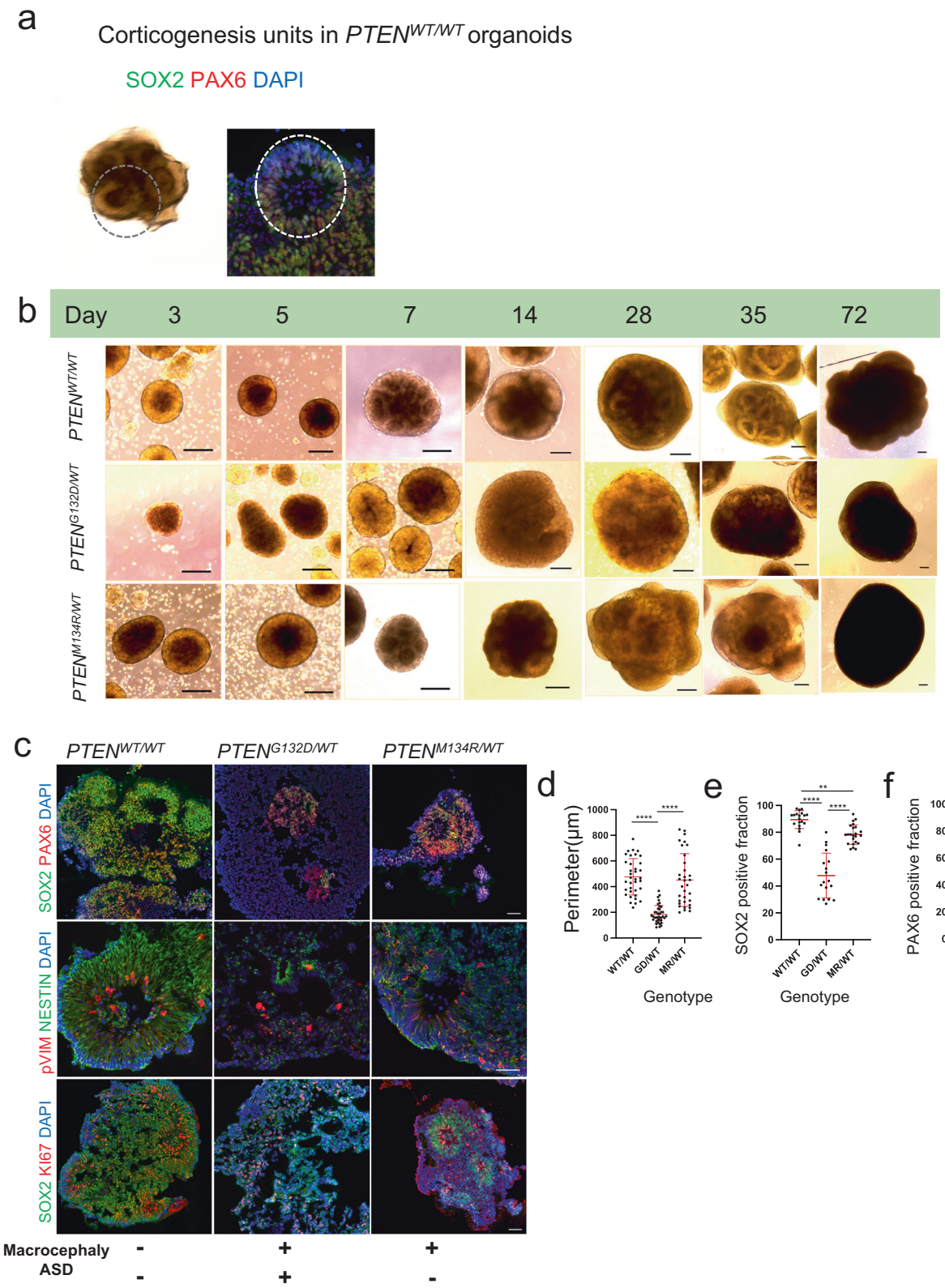

were assessed for the expression of the pan-neuronal marker, TUJ1, which marks immature post-mitotic neurons (Fig. 3a) [47]. On day 28, TUJ1$^+$ layering in *PTEN*$^{WT/WT}$ organoids was the thickest amongst all three genotypes, p-value = 0.0001, and continued to increase in size from day 28 to day 72 by 2.5-fold, p-value < 0.0001 (Fig. 3b). The thickness of the TUJ1$^+$ cell layer increased by day 72 in *PTEN*$^{G132D/WT}$ organoids as well, but to a lesser extent compared to *PTEN*$^{WT/WT}$ organoids, p-value < 0.0001 (Fig. 3b). In contrast, the TUJ1$^+$ cell layer thickness did not increase during this period in *PTEN*$^{M134R/WT}$ organoids compared to *PTEN*$^{WT/WT}$, p-value < 0.0001 (Fig. 3b).

Fig. 2 Morphological defects in cellular organization and patterning observed in mutant *PTEN* corticogenesis unit. a Phase contrast image of a $PTEN^{WT/WT}$ organoid at day 14, shows corticogenesis unit structure as indicated by a broken white outline circle (left panel). Immunofluorescence staining detected SOX2 and PAX6 positive cells arranged in a circular pattern within of the corticogenesis unit outlined in broken white outline (right panel). **b** Representative phase contrast images of $PTEN^{WT/WT}$, $PTEN^{G132D/WT}$ and $PTEN^{M134R/WT}$ forebrain organoids at days 3, 5, 7, 14, 28, and 35. Scale bars indicates 200 µm. **c** IF staining of neural progenitor markers (SOX2, PAX6, and NESTIN), neuroepithelial glial (pVIM) and proliferating cells (KI67) in $PTEN^{WT/WT}$, $PTEN^{G132D/WT}$, and $PTEN^{M134R/WT}$ organoids on day 14. Scale bars indicate 50 µm, representative images have been brightened for improved visual clarity. **d** Quantification of the $SOX2^+$ IF perimeter within corticogenesis units at day 14. Values represent mean ± SEM: $PTEN^{WT/WT}$ (WT/WT) 476.0245 µm ± 141.83608, $n = 36$ corticogenesis units from six organoids; $PTEN^{G132D/WT}$ (GD/WT) 184.598 µm ± 68.879, $n = 38$ corticogenesis units from eight organoids; $PTEN^{M134R/WT}$ (MR/WT) 452.1 µm ± 205.3, $n = 33$ corticogenesis units from five organoids; $F = 45.06$, p-value = 0,045, p-value < 0.0001. **e** Percentages of neural progenitor cells positive for SOX2; $PTEN^{WT/WT}$ (WT/WT) 91.72% ± 6.31, $PTEN^{G132D/WT}$ (GD/WT) 38.452% ± 18.877, p-value < 0.0001; $PTEN^{M134R/WT}$ (MR/WT) 77.53% ± 6.99, $n = 18–21$ corticogenesis units from more than 6 organoids; $F = 73.42$, p-value = 0.0001. **f** Percentages of neural progenitor cells positive for PAX6 were; $PTEN^{WT/WT}$ (WT/WT) 91.337% ± 4.33, $PTEN^{G132D/WT}$; (GD/WT) 12.898% ± 7.504, $PTEN^{M134R/WT}$ (MR/WT) 67.116% ± 12.318, $n = 18–21$ corticogenesis units from more than 6 organoids; $F = 119.2$, p-value < 0.0001. *<0.05, **<0.01, ***<0.001, ****<0.0001.

Next, we used IF to determine if the two *PTEN*-mutant alleles affected the development and patterning of intermediate neurons by day 28 and 72. $TBR1^+$ intermediate neurons are reported to emerge from $PAX6^+$ cortical lineal precursor cells that reside in the area which is considered to be the subventricular zone (SVZ) in forebrain organoids [38, 40, 48]. On day 28 we observed $TBR1^+$ neurons in $PTEN^{WT/WT}$ organoids evenly distributed throughout corticogenesis units (Fig. 3c). By day 72, $TBR1^+$ neurons increased in number forming a structure reminiscent of SVZ by clustering outside of the VZ-like structure, which is occupied by $SOX2^+$ NPCs in $PTEN^{WT/WT}$ organoids (Fig. 3c, d). We quantified the number of $TBR1^+$ neurons per corticogenesis units and found a 4.4-fold increase from day 28 to day 72, p-value < 0.0001 (Fig. 3d). Next, we assessed $PTEN^{G132D/WT}$ and $PTEN^{M134R/WT}$ organoids on day 28 and found the arrangement of $TBR1^+$ cells were significantly disorganized in $PTEN^{G132D/WT}$ organoids with respect to their positioning to $SOX2^+$ cells (Fig. 3c). Furthermore, assessment of $TBR1^+$ cells in $PTEN^{G132D/WT}$ and $PTEN^{M134R/WT}$ organoids on day 72 showed no signs for further expansion in cell number or improvement of organization, with respect to their positioning to $SOX2^+$ cells (Fig. 3c). In $PTEN^{M134R/WT}$ organoids, the arrangement of $TBR1^+$ cells in $PTEN^{M134R/WT}$ on day 28 was similar to $PTEN^{WT/WT}$, as TBR1+ cells were positioned more proximally to $SOX2^+$ cells compared to $PTEN^{G132D/WT}$ organoids. This cellular organizational similarity to $PTEN^{WT/WT}$ organoids was completely lost on day 72 (Fig. 3c). We then observed that the number of $TBR1^+$ cells per corticogenesis unit in both *PTEN*-mutant genotypes $PTEN^{G132D/WT}$ and $PTEN^{M134R/WT}$ were significantly lower compared to those of $PTEN^{WT/WT}$ on day 28, and by day 72, p-value < 0.0001 (Fig. 3d). These data demonstrate that mutant $PTEN^{G132D}$ allele disrupted the development and cortical patterning / migration of $TBR1^+$ cells at the earlier developmental stage compared to the $PTEN^{M134R}$ allele.

Furthermore, to determine if there may be impaired neurodevelopment and maturation in the mutant organoids, we utilized electrophysiological recordings to examine the effects of the *PTEN* mutations on the maturation of NPCs during the early stages of development. We found that on day 7 and day 14, both $PTEN^{WT/WT}$ and $PTEN^{M134R/WT}$ NPCs showed depolarization-activated inward currents (Fig. 3e) which had typical current/voltage (I/V) curve of voltage-gated sodium channels (Na_V) (Fig. 3f). The sodium current (I_{Na}) of $PTEN^{M134R/WT}$ was significantly smaller than $PTEN^{WT/WT}$ on day 7, p-value = 0.0419, but was comparable on day 14, suggesting a delayed but eventually catching up development of $PTEN^{M134R/WT}$ NPCs. The I_{Na} could generate subthreshold single sodium-spike at current-clamp but not sufficient for action potential (AP) generation in both genotypes (Fig. 3g). However, on day 21, we were able to record larger I_{Na} and AP firing from both $PTEN^{WT/WT}$ and $PTEN^{M134R/WT}$, indicating continuous maturation of NPCs in these two genotypes (Fig. 3e–g). To our surprise, almost no I_{Na} could be recorded from $PTEN^{G132D/WT}$ NPCs on all three tested timepoints (Fig. 3e–g). This observation was further validated by immunostaining of $Na_V1.1$, the major Na_V subunit expressed in the neuron. The result showed that $Na_V1.1$ was found in some of the $PTEN^{WT/WT}$ and $PTEN^{M134R/WT}$ NPCs but not in $PTEN^{G132D/WT}$ NPCs (Fig. 3h), in agreeance with the electrophysiological data. These data suggest that the NPCs maturation is comparable between $PTEN^{WT/WT}$ and $PTEN^{M134R/WT}$ genotypes but is significantly delayed in $PTEN^{G132D/WT}$ genotype. These data, also suggest that mutant alleles associating with distinct clinical phenotypes differently impact, not only neuronal differentiation and post-mitotic neuronal migration, but also function.

Mutant *PTEN* alleles disrupt the neural tube lumen morphology and radial glial cell patterning in corticogenesis units

The cellular processes of RGCs are essential for the formation of cortical layers as they act as a "road-map" that guide post-mitotic neurons to migrate from the SVZ to their destinations in the cortical layers, thus forming the cortex [49, 50]. The $PTEN^{M134R}$ and $PTEN^{G132D}$ alleles disrupt cortical neural layer formation, as demonstrated by the disorganization and lack of $TUJ1^+$ and $TBR1^+$ cell layers surrounding $SOX2^+$ cells in our forebrain organoids (Fig. 3). We speculated if the dysfunctional cortical layer formation was due to the malformed neural tube, which otherwise serves as the foreground of RGC positioning along the SVZ [51]. To visualize the neural tube-like structure of the corticogenesis unit in the organoids, we performed IF staining for β-CATENIN and Zonular occludens-1 (ZO-1), a maker expressed at the apical region of the neural tube lumen (Figs. 4a and S2). We collected FB organoid on days 3, 5, 6, and 7 to examine if $PTEN^{G132D}$ organoids showed any signs of disruption in early neural tube formation that may cause corticogenesis unit malformation at later stages (Fig. 2b, c). We observed that $PTEN^{WT/WT}$ and $PTEN^{M134R/WT}$ neuroepithelium formed a symmetrical and circular lumen at days 6 and 7, while $PTEN^{G132D/WT}$ organoids formed a narrow and elliptical luminal shape (Fig. 4a). At day 7 we observed that ZO-1 staining co-localizes with β-CATENIN in $PTEN^{WT/WT}$ and $PTEN^{M134R/WT}$ neuroepithelium, however, ZO-1 expression was only observed on the outer surface and luminal area of the $PTEN^{G132D/WT}$ organoid at day 7, and was visually more intense compared to $PTEN^{WT/WT}$ and $PTEN^{M134R/WT}$ (S2).

Next, we analyzed the development of RGCs by IF staining for the RGC marker pVIMENTIN (pVIM). $pVIM^+$ cells were detected in organoids of all genotypes by day 5 and appeared to be morphologically indistinguishable from one another (Fig. 4b). In $PTEN^{WT/WT}$ and $PTEN^{M134R/WT}$ organoids, the $pVIMENTIN^+$ cells were apically aligned around the lumen of the neural tube-like structure by day 7 and remained this way through day 14, when they developed projections extending towards the SVZ-like area (Fig. 4b). By day 72, $pVIM^+$ cells in $PTEN^{WT/WT}$ organoids were well aligned around the VZ-like structure comprising $NESTIN^+$ cells (Fig. 4b, c). In $PTEN^{M134R/WT}$ organoids on day 72, however, we could no longer

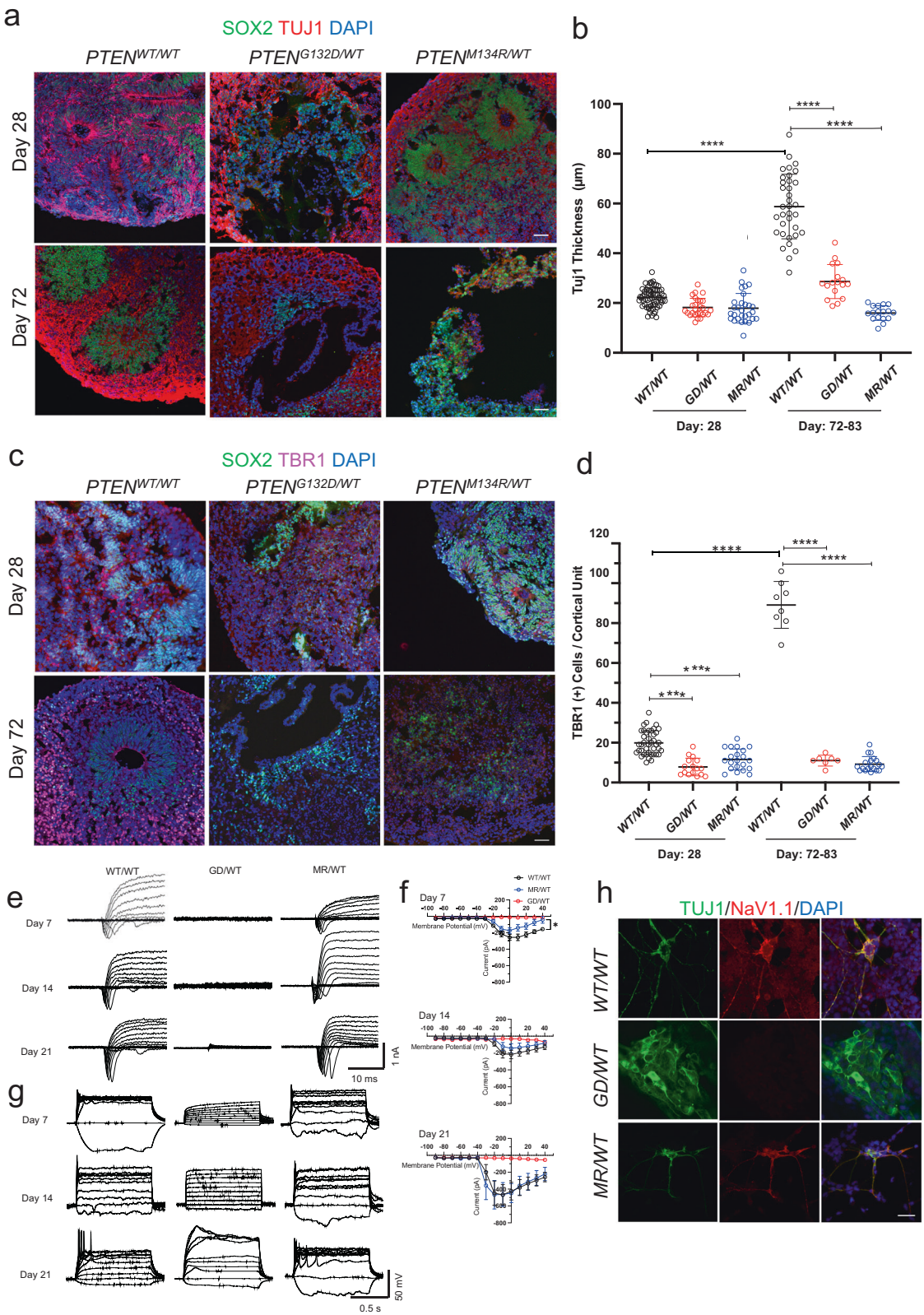

detect the well aligned pVIM^{+} cell organization, which was observed on day 7 and day 14 (Fig. 4b). Conversely, we sparsely observed well-oriented pVIM^{+} cell organization in *PTEN*$^{G132D/WT}$ organoids, and there was considerably less expression and organization of NESTIN^{+} cells making up the corticogenesis unit (Fig. 4b). Furthermore, in *PTEN*$^{G132D/WT}$ organoids, we did not observe organized alignment of pVIM^{+} cells around what would be the VZ-like structure. Despite the presence of pVIM^{+} cells at days 14 and 72, they remained disorganized and irregularly located thought the corticogenesis units of the *PTEN*$^{G132D/WT}$ organoid (Fig. 4b).

Fig. 3 Neuronal maturation is impaired in ASD-associated *PTEN*$^{G132D/WT}$ organoids and delayed maturation of *PTEN*$^{G132D/WT}$ brain organoid compared to *PTEN*$^{WT/WT}$ and *PTEN*$^{M134R/WT}$. **a** IF staining of neural progenitor (SOX2) and postmitotic neurons (TUJ1 cells) in forebrain organoids of *PTEN*$^{WT/WT}$, *PTEN*$^{G132D/WT}$, and *PTEN*$^{M134R/WT}$ at day 28 and 72. **b** Quantified thickness of peripheral TUJ1^{+} cell surrounding SOX2^{+} neural progenitors at day 28 and day 72. Values represent means ± SEM; *PTEN*$^{WT/WT}$ (WT/WT) 22.243 µm ± 3.9 at day 28 and 58.51 µm ± 12.971 at day 72, $n = 27$ corticogenesis units from four organoids, *PTEN*$^{G132D/WT}$ (GD/WT) 18.181 µm ± 3.72, $n = 9$ corticogenesis units from three organoids, *PTEN*$^{M134R/WT}$ (MR/WT) 17.923 µm ± 5.9, $n = 14$ corticogenesis units from five organoids; $F = 177.9$, p-value < 0.0001. Scale bars indicate 50 µm. *<0.05, **<0.01, ***<0.001, ****<0.0001. **c** IF staining of SOX2^{+} neural progenitor cells and cortical layer TBR1^{+} neurons in *PTEN*$^{WT/WT}$, *PTEN*$^{G132D/WT}$, and *PTEN*$^{M134R/WT}$ forebrain organoids at day 28 and 72. **d** Quantification of TBR1^{+} cells per corticogenesis unit at day 28 and day 72. Values represent means ± SEM; *PTEN*$^{WT/WT}$ (WT/WT) 19.902 ± 6.01 at day 28, 87.75 ± 11.77 at day 72, $n = 4$ organoids; *PTEN*$^{G132D/WT}$ (GD/WT) 8.071 ± 4.75 at day 28, 11 ± 2.7 at day 72, $n = 3$ organoids; *PTEN*$^{M134R/WT}$ (MR/WT), 13.31 ± 4.33 at day 28, 9.263 ± 3.7 at day 72, $n = 4$ organoids; $F = 265.8$, p-value < 0.0001. Scale bars indicate 50 µm. **e** Representative traces showing I_{Na} recorded from *PTEN*$^{WT/WT}$, *PTEN*$^{G132D/WT}$, and *PTEN*$^{M134R/WT}$ NPC cultures on day 7, day 14, and day 21. **f** Summarized current/voltage (I/V) curves reveal the activation/inactivation properties of I_{Na} recorded from *PTEN*$^{WT/WT}$, *PTEN*$^{G132D/WT}$, and *PTEN*$^{M134R/WT}$ NPC cultures on day 7 ($n = 6$, 5, and 6 NPCs respectively), day 14 ($n = 7$, 5, and 6), and day 21 ($n = 8$ for all three genotypes). *<0.05. **g** Representative traces showing changes of membrane potentials following step-current injection of *PTEN*$^{WT/WT}$, *PTEN*$^{G132D/WT}$, and *PTEN*$^{M134R/WT}$ NPC cultures on day 7 (top), day 14 (middle), and day 21(bottom). **h** Representative images of neurons expressing neuronal marker, TUJ1 (green) and sodium channel marker, $Na_V1.1$(red). Scale bar indicates 50 µm. *<0.05, **<0.01, ***<0.001, ****<0.0001.

Increased AKT activation and persistence of stemness of *PTEN*$^{G132D/WT}$ organoids and dysregulation of N- and E-Cadherin

PTEN regulates many important biological processes by antagonizing PI3K/AKT signaling through its lipid phosphatase activity [52–55]. Certain *PTEN* mutations have been shown to reduce the overall expression and phosphatase activity of PTEN [56, 57]. Here, we examine how the *PTEN*^{G132D} and *PTEN*^{M134R} alleles affect PTEN expression and PI3K/AKT signaling during the first 7 days of organoid development compared to that of *PTEN*$^{WT/WT}$. Western blot analysis detected similar levels of PTEN expression between *PTEN*$^{WT/WT}$ and *PTEN*$^{M134R/WT}$ organoids, but statistically significant lower levels of PTEN expression was detected in *PTEN*$^{G132D/WT}$ organoids, p-value < 0.0001, on day 7 compared to controls (Fig. 4d, e). Next, we evaluated canonical PTEN signaling using Western blot. We found that *PTEN*$^{G132D/WT}$ organoids expressed increased levels of phosphorylated AKT(S473) (pAKT* unless otherwise stated) when normalized to overall AKT expression at day 5 when compared to *PTEN*$^{WT/WT}$ organoids, p-value = 0.003 (Fig. 4d, e). In contrast, pAKT expression was decreased in *PTEN*$^{WT/WT}$ organoids by day 3 and became almost undetectable by day 6 (Fig. 4d, e). In *PTEN*$^{M134R/WT}$ organoids, pAKT expression did not begin to decline until day 5, while the overall pAKT expression levels were higher in *PTEN*$^{M134R/WT}$ organoids compared to *PTEN*$^{WT/WT}$, but lower than *PTEN*$^{G132D/WT}$ organoids during days 0–7 (Fig. 4d, e). Additionally, we performed Western blots from day 0 through 7 organoids to examine the expression of pAKT(T308), pS6, and 4EB-P1, as these represent significant downstream effector molecules of PTEN signaling. However, we found no significant or remarkable changes in protein expression of ether molecule between genotypes during early development (Fig. S3a–d).

Next, we examined the expression of E-CDH (Epithelial CADHERIN) and N-CDH (Neuronal CADHERIN) as their expression are essential in the establishment of the 3 germ layers, and cellular migration required for organ development to begin [58]. To determine if pluripotent stem cells who express E-CDH were differentiating into neuroepithelium that expressed N-CDH, we utilized immunofluorescence (IF) to stain N-CDH in organoids from all three genotypes on day 7 (Fig. 4f). Both *PTEN*$^{WT/WT}$ and *PTEN*$^{M134R/WT}$ organoids had clear N-CDH expression around the lumen area of their corticogenesis units. However, N-CDH expression was not detected in *PTEN*$^{G132D/WT}$ organoids (Fig. 4f). Next, we confirmed E-CDH and N-CDH expression during early organoid development by Western blot (Fig. 4g). We observed that E-CDH expression sharply decreased in both *PTEN*$^{WT/WT}$ and *PTEN*$^{M134R/WT}$ organoids by day 5 with reciprocal increase in N-CDH expression (Figs. 4g, and S4a and b). During 7days of *PTEN*$^{G132D/WT}$ FB organoid derivation little change was observed in E-CDH expression levels which were comparable to the levels observed in those of organoids of other genotypes on day 0, while minimal induction of N-CDH at delayed timing starting on day 5 was detected (Figs. 4g, and S4a, b). The blockade of E to N-CDH switch suggests that disruption of forebrain organoid induction may be caused by the defect of the transition from pluripotent stem cell to neuroepithelium in *PTEN*$^{G132D/WT}$ organoids, as it is reported that the lack of PTEN increases AKT signaling which promotes stem cell-state maintenance [39].

Inhibition of AKT restores lumen morphology and neuroepithelial cell alignment in the early stage of forebrain formation in *PTEN*$^{G132D/WT}$ organoids

Western blot detected the highest levels of the pAKT in *PTEN*$^{G132D/WT}$ organoids showing the most severe deviations from FB organoids in *PTEN*$^{WT/WT}$ during the first 7-day induction period (Fig. 4a, b, and d). To determine if AKT inhibition could potentially rescue the abnormal lumen morphology observed in *PTEN*$^{G132D/WT}$ organoids (Fig. 4a, b), we added 1 µM of the AKT inhibitor Perifosine to forebrain induction medium during days 0–7. We confirmed that Perifosine treatment resulted in considerable suppression of AKT activation in *PTEN*$^{WT/WT}$, *PTEN*$^{G132D/WT}$, and *PTEN*$^{M134R/WT}$ as shown by overall sustained decreased levels in pAKT expression from days 3 to 7 (Fig. 5a, S5b), as well as no impact on overall PTEN levels (Figs. 5a, S5a). The overall reduction in pAKT in *PTEN*$^{G132D/WT}$ and *PTEN*$^{M134R/WT}$ organoids was visually observable via Western blot when compared to *PTEN*$^{WT/WT}$ organoids treated with Perifosine, especially at days 5, 6, and 7 (Figs. 5a, S5b). Although Perifosine treatment resulted in considerable suppression of AKT activation in organoids of all three genotypes from days 3 to 7 (Figs. 5a, S5b), this treatment was not sufficient to decrease E-CDH expression in *PTEN*$^{G132D/WT}$ organoids (Figs. 5a, S5c). In fact, *PTEN*$^{G132D/WT}$ E-CDH and N-CDH expression remained unchanged over time in the presence of Perifosine (Figs. 5a, S5c, d). However, this was accompanied by a drastic decrease in *PTEN*$^{WT/WT}$ and *PTEN*$^{M134R/WT}$ E-CDH levels from days 5–7 (Fig. 5a). We additionally examined if there were changes in the mTORC2 substrate SGK-1 (pSGK-1) to determine if this may be a mechanism involved in regulating the N / E cadherin shift we had observed in Fig. 4g. However, we did not observe any changes in SGK-1 phosphorylation in the presence of Perifosine in any of the genotypes (Fig. S4c and S4d). These data suggesting a mTORC2-independent mechanism may be responsible for the dysregulation of N / E Cadherin shift in both mutant genotypes.

Next, we treated organoids with Perifosine to determine if AKT inhibition could restore the irregular lumen morphology observed in *PTEN*$^{G132D/WT}$ organoids. For clarity, we define the radial glial VZ-like structure with white dotted lines (Fig. 5b). In *PTEN*$^{G132D/WT}$ organoids with Perifosine treatment, we observed the formation of circular lumens that were nearly indistinguishable from those of *PTEN*$^{WT/WT}$ by day 7 (Fig. 5c). Compared to *PTEN*$^{G132D/WT}$ organoids without Perifosine treatment, pVIM^{+} cells positioned around the apical surface of the lumen and lumen surface demonstrated by the patterning of ZO-1^{+} cells (S6a and S6d). Next, we quantified the

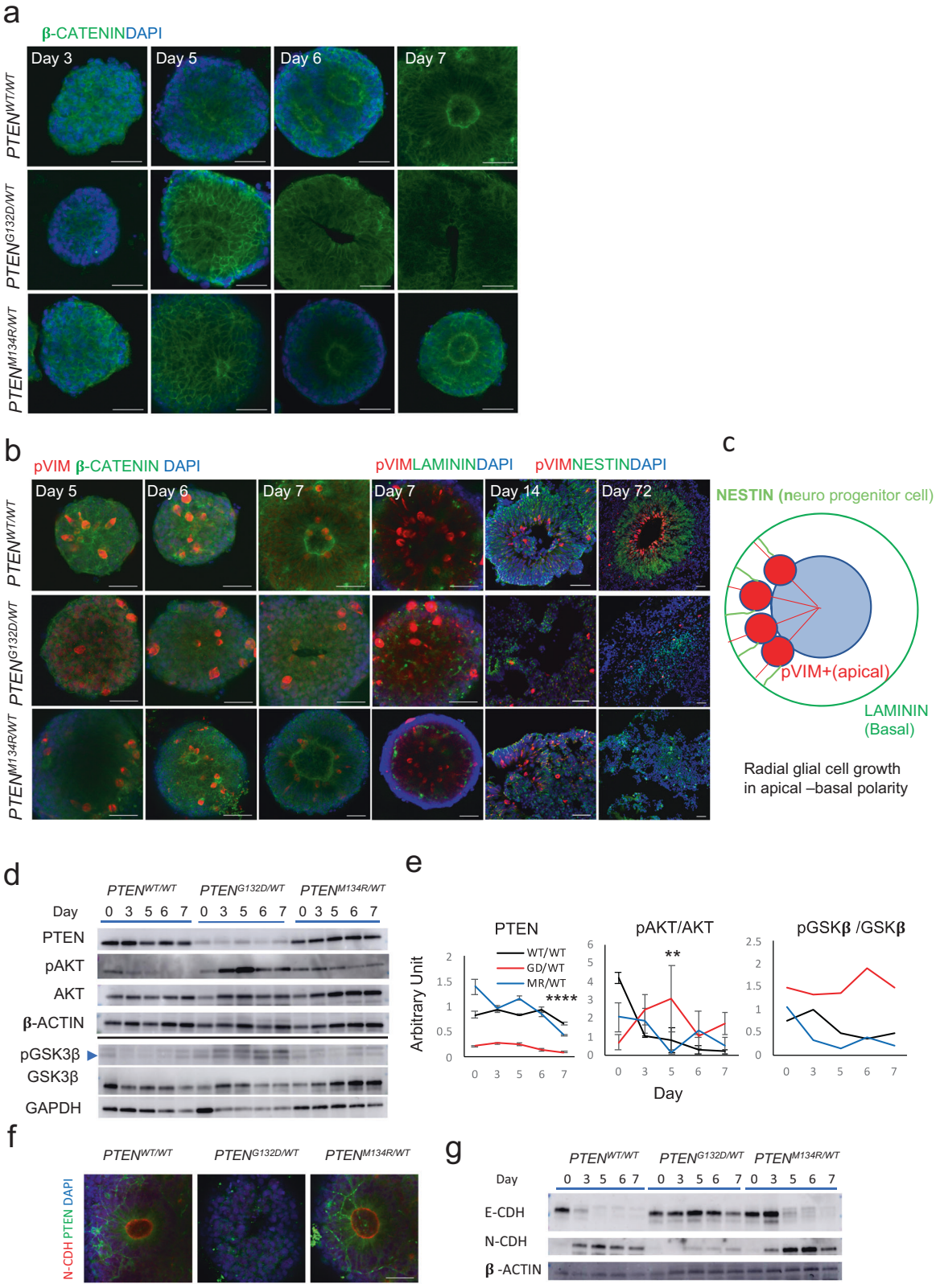

extent to which the malformed neural tube lumen had been rescued by Perifosine treatment in *PTEN*$^{G132D/WT}$ organoids by measuring the circularity of the lumen circumference using the ZO-1 and β-CATENIN-stained organoids on day 7 (Figs. 5b, c, S6d). The lumen circularity of *PTEN*$^{WT/WT}$ and *PTEN*$^{M134R/WT}$ organoids was very similar with an average value of ~0.8 regardless of Perifosine treatment compared to *PTEN*$^{G132D/W}$ organoids showing average circularity = 0.6 ± 0.193, an indicative of non-circular structure, *p*-value = 0.0496, *p*-value < 0.0001 (Figs. 5c, S6d). When incubated with Perifosine, we observed a partially rescued phenotype of the lumen structure, resulting in a more symmetrical, circular shape, and relatively more homogenous *PTEN*$^{G132D/WT}$ neural tube lumen

Fig. 4 VZ-like lumen morphology and radial glial patterning are disrupted during early development as well as activated AKT signaling in early mutant *PTEN* organoid development. a IF staining of β-Catenin in $PTEN^{WT/WT}$, $PTEN^{G132ED/WT}$, and $PTEN^{M134R/WT}$ organoids at days 3, 5, 6, and 7. Scale bars indicate 50 µm. **b** IF staining of pVIM and β–CATENIN in developing organoids at days 5, 6, 7, 14, and 72. Scale bars indicate 50 µm. **c** Schematic illustrating normal radial glial cell growth in apical (pVIM) and basal (LAMININ) polarity. **d** Representative Western blot for PTEN, AKT, and GSK3β signaling at the early stages of forebrain organoid development. β-Actin and GAPDH was used as a loading control respectively. **e** Quantification of biological replicate Western blots for PTEN expression from Fig. 4d ($n = 3$). Values represent means ± SEM; PTEN expression at day 7 in $PTEN^{WT/WT}$ (WT/WT) 0.658 ± 0.03, $PTEN^{G132D/WT}$(GD/WT) 0.1038 ± 0.016, $PTEN^{M134R/WT}$ (MR/WT) 0.4395 ± 0.029; $F = 109.2$, p-value < 0.0001, $n = 3$. Also, quantification of $n = 3$ biological replicate Western blots for pAKT expression from Fig. 4d ($n = 3$). Values represent means ± SEM; pAKT expression at day 5 in $PTEN^{WT/WT}$ (WT/WT) 0.504 ± 0.02, $PTEN^{G132D/WT}$(GD/WT) 1.526 ± 0.118, $PTEN^{M134R/WT}$ (MR/WT) 0.0492 ± 0.006; $F = 8.105$, p-value < 0.0026, $n = 3$. **f** IF staining of N-CDH (Neuronal CADHERIN) at day 7 in $PTEN^{WT/WT}$, $PTEN^{G132ED/WT}$, and $PTEN^{M134R/WT}$ organoids. Scale bars indicate 50 µm. **g** Western blot of E-CDH (Epithelial CADHERIN) and N-CDH during organoid induction at days 0, 3, 5, 6, and 7. *<0.05, **<0.01, ***<0.001, ****<0.0001.

with average circularity >0.7 ± 0.121, p-value < 0.0001 (Figs. 5c, S6d). Furthermore, we measured the thickness of VZ-like structures at day 7 to determine if daily growth of VZ was impaired by mutant *PTEN* alleles from days 5, 6, and 7 of FB organoid derivation (Fig. 5d). As compared to $PTEN^{WT/WT}$ organoids, we observed a delay in the rate of VZ expansion in $PTEN^{G132D/WT}$ organoids through days 5, 6, and 7 in the absence of Perifosine. $PTEN^{G132D/WT}$ organoid VZ thickness increased from day 5 to day 6, p-value = 0.0152, and from day 6 to day 7, p-value < 0.0001, in the presence of Perifosine resulting in two-fold increase from day 5 to day 7, p-value < 0.0001 (Fig. 5d). On day 7 their thickness became indistinguishable from those of $PTEN^{M134R/WT}$ organoids and thicker than $PTEN^{WT/WT}$ organoids, p-value < 0.0001 (Fig. 5d). The increase of VZ thickness was also increased in $PTEN^{M134R/WT}$ organoids with Perifosine treatment as indicated by a substantial increase reaching a plateau on day 5, and remined the overall largest in thickness with and without Perifosine treatment compared to all over genotypes (Fig. 5d). Furthermore, the VZ-like thickness in $PTEN^{G132D/WT}$ treated with Perifosine became thicker than that of $PTEN^{WT/WT}$ organoids with and without Perifosine on day 7, p-value < 0.0001 (Fig. 5d). These data demonstrate that PTEN dependent regulation of AKT signaling may modulate the formation and growth of neuroepithelium.

Furthermore, we also examined radial glia patterning at day 7 with and without Perifosine to determine if AKT inhibition could also rescue circularity and thickness of $PTEN^{G132D/WT}$ organoid (Fig. S6a, b). Here, we show that the distance of radial glia from the central lumen is significantly higher in $PTEN^{G132D/WT}$ organoid compared to $PTEN^{WT/WT}$ and $PTEN^{M134R/WT}$ (Fig. S6b, c) where AKT is not inhibited. However, when grown in the presence of Perifosine the distance of the radial glia significantly drops and becomes more organized and tightly packed around the luminal center of $PTEN^{G132D/WT}$ organoids, becoming similar to $PTEN^{WT/WT}$ and $PTEN^{M134R/WT}$ (Fig. S6b, c). These data suggest that pAKT plays a significant role in regulating the cellular organization, circularity, and thickness of organoids during early development.

AKT inhibition upregulates neural fate associated transcriptome

After finding that AKT inhibition was sufficient in partially rescuing the cellular disorganization phenotypes to varying extents in both mutant organoids, we decided to perform single cell RNA sequencing (scRNAseq) to assess the transcriptomic profiles associated with the different genotypes and how Perifosine treatment alters these profiles. The transcriptomic profiles are presented in Uniform Manifold Approximation and Projection (UMAP) (Fig. 5e). We attempted to assess cell identities after cell clustering (Fig. 5f), but it was very difficult to establish cellular identities based on specific cell markers since the analyzed cell populations were in the very early stages of neuroectodermal differentiation. Therefore, we decided to use the monocle3 tool to analyze the pseudotime in differentiation trajectory of the clustered cells and found a striking difference between the $PTEN^{G132D/WT}$ genotype and other two genotypes, $PTEN^{WT/WT}$ and $PTEN^{M134R/WT}$ (Fig. 5g). $PTEN^{G132D/WT}$ organoids fail to mature compared to those of the other genotypes in the pseudotime scale and maintain a pluripotent stem cell transcriptomic pattern. Using scRNAseq we detected lower E-CDH and higher N-CDH transcripts in day 7 $PTEN^{WT/WT}$ and $PTEN^{M134R/WT}$ organoids than in $PTEN^{G132D/WT}$ organoids (Fig. 5h). This observation was consistent with Western blot analysis indicating cadherin switch failed in $PTEN^{G132D/WT}$ organoids (Figs. 4g, S4a and b). We also assessed if AKTi treatment promoted the cadherin expression shift from E-CDH to N-CDH in the $PTEN^{G132D/WT}$ but found no significant changes in gene expression (Fig. 5h–j).

We further analyzed the dataset using Ingenuity Pathway Analysis (IPA) tool. We performed a differentially expressed gene (DEG) analysis of each sample against the entire gene expression dataset from all combined samples, as well as against each other within the dataset (Figs. S7, S8). We loaded the DEGs into the IPA pipeline and found that several pathways relating to pluripotency signatures were upregulated in $PTEN^{G132D/WT}$ when compared against the entire dataset (Fig. 5e). However, when we performed the same comparison using the data set from AKTi treated $PTEN^{G132D/WT}$ organoids, we found an enrichment of pathways associating with neural functions such as "Outgrowth of neurons," "Outgrowth of neurites", "Microtubule dynamics" among others (Fig. 5l). We performed a direct comparison of DEG between $PTEN^{G132D/WT}$ with and without AKTi treatment and found that AKTi treatment upregulated transcriptomic signatures related to neural fate commitment in the treated group (Fig. 5m).

Moreover, when we examined pathways related to development and function of the nervous system in this data set, we saw a predicted upregulation of certain functions such as "Differentiation of neural precursor cells" or "Morphology of the nervous system" (Fig. S9b). Most of these observations were based on ID1 and ID3 transcriptomic status among other molecules (Fig. S9c). Additionally, we also measured the transcriptomic levels of neuroectodermal markers PAX6 and SOX2, as well as proliferation marker KI67. We observed high KI67 and low PAX6 and SOX2 in the $PTEN^{G132D/WT}$ organoids when compared with $PTEN^{WT/WT}$ and $PTEN^{M134R/WT}$ organoids further supporting a disruption in neuroectodermal differentiation and cell proliferation (Fig. S9a). Overall, these findings suggest that AKT inhibition transcriptomically promotes the expression of pathways pertaining to neural differentiation. However, we also observed that AKT inhibitor treatment alone was not sufficient to correct the deficits observed in E-CDH to N-CDH expression shift, or other critical events of neural development in $PTEN^{G132D/WT}$ organoids.

DISCUSSION

The critical roles of *PTEN* during embryonic development and embryonic stem cell biology have been demonstrated by gene knockout studies [59, 60]. This study reveals a connection between *PTEN*-mutant alleles, which are linked to varying clinical phenotypes in PHTS patients, and their influence on neurodevelopmental processes. These impacts are replicated within the brain organoid model, displaying differing levels of severity. The $PTEN^{G132D/WT}$ genotype (associated with ASD) more severely disrupted brain organoid development compared to $PTEN^{M134R/WT}$ (no association

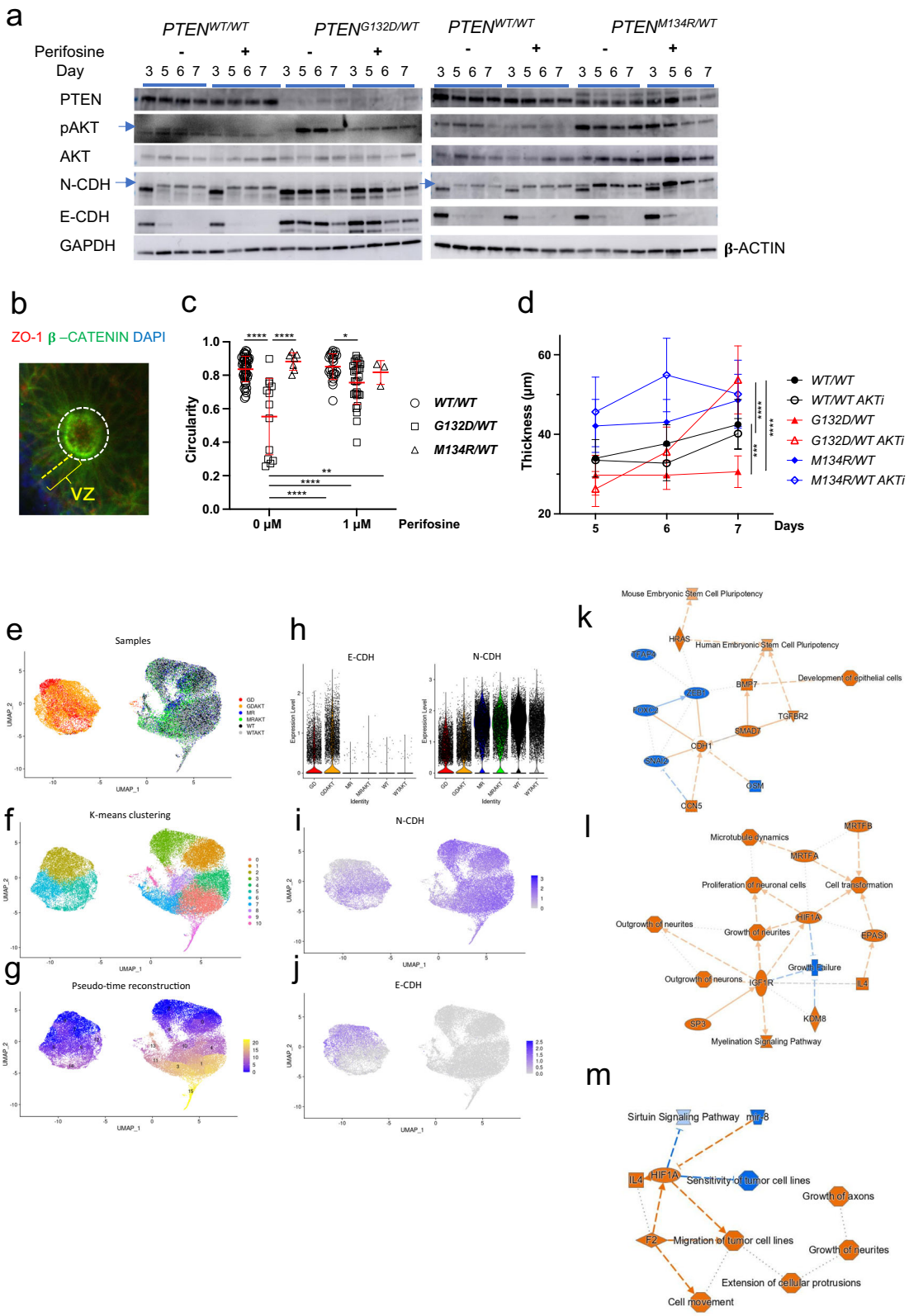

with ASD phenotype). Our data show that *PTEN* is an essential regulator of early brain development by driving the initial differentiation of neuroectoderm, as well as an essential regulator of early neuronal migration and organization. Although PTEN has multiple functions, we surmise that the phosphatase activity of PTEN plays critical roles in neurodevelopmental processes and is essential for transitioning neuro-stem cells to a post mitotic and mature state necessary for the development of neurons. AKT is activated when the phosphatase activity of PTEN is compromised as we observed in FB organoids with the *PTEN*^{G132D} mutant allele.

Fig. 5 PAKT regulates lumen morphology and neuroepithelial cell alignment in *PTEN*$^{G132D/WT}$ organoids. **a** Representative Western blot of PTEN, pAKT, AKT, E-CDH, and N-CDH expression from organoids grown in the presence of Perifosine at days 3, 5, 6, and 7; comparing *PTEN*$^{WT/WT}$ and *PTEN*$^{G132D/WT}$ ($n = 3$) as well as *PTEN*$^{WT/WT}$ and *PTEN*$^{M134R/WT}$ ($n = 2$). **b** IF staining of β–CATENIN and ZO-1 showing lumen shape used for measuring circularity and ventricular zone (VZ) for the measurement of the thickness. **c** Analysis examining lumen circularity of day 7 organoids. We performed a 2-way ANOVA to determine if there were any changes in lumen circularity. Values represent means ± SEM; *PTEN*$^{WT/WT}$ 0.8366 ± 0.0765 (WT/WT), 0.85 ± 0.075 (WT/WT AKTi); *PTEN*$^{G132D/WT}$ 0.575 ± 0.193 (GD/WT), 0.765 ± 0.121 (GD/WT AKTi); *PTEN*$^{M134R/WT}$ 0.8816 ± 0.0669 (MR/WT), 0.873 ± 0.061 (MR/WT AKTi), $n = 10$–34 cortical structures from more than 6 organoids per genotype; $F = 25.71$, p-value < 0.0001, p-value = 0.0496. **d** Graphed neuroepithelial apical and basal cell growth changes at the early stage of formation of corticogenesis unit from day 5 to day 7. Quantification of distance from the ventricular zone (VZ) to the surface of the lumen in *PTEN*$^{WT/WT}$ (WT/WT), *PTEN*$^{G132D/WT}$ (GD/WT), and *PTEN*$^{M134R/WT}$ (MR/WT) organoids. Analyzed with 2-way ANOVA, values represent ±SEM, VZ thickness at day 7 *PTEN*$^{WT/WT}$ 42.48 ± 6.2 (WT/WT), 40.19 ± 3.806 (WT/WT AKTi); *PTEN*$^{G132D/WT}$ 30.62 ± 3.975 (GD/WT), 53.70 ± 8.57 (GD/WT AKTi); *PTEN*$^{M134R/WT}$ 48.55 ± 6.568 (MR/WT), 50.11 ± 8.549 (MR/WT AKTi), $n = 3$–13 corticogenesis units from $n = 3$–8 organoids per genotype; $F = 32.45$, p-value < 0.0001, p-value = 0.0152. **e** UMAP of scRNAseq experiment of neuroepithelial organoids at day 7 (colors represent each genotype with and without AKTi treatment). **f** Clustering of single cell dataset using unsupervised k-means method. **g** Pseudo time scale reconstruction of scRNAseq data set. **h** Violin plot depicting differences in E-cadherin and N-cadherin normalized expression in the different samples. **i, j** Above (as in **h**) E-cadherin and N-cadherin normalized expression plotted in the UMAP topology. **k** Ingenuity pathway analysis (IPA) of (WT/GD) gene expression compared to the complete data set gene expression (orange depicts pathways upregulated in (WT/GD) and blue depicts downregulated pathways). **l** IPA of (WT/GD) with AKTi treatment expression pattern compared to the complete data set gene expression (orange depicts pathways upregulated in (WT/GD) with AKTi and blue depicts downregulated pathways). **m** IPA of differentially expressed genes in a direct (WT/GD) vs (WT/GD AKTi) comparison (orange depicts pathways upregulated in (WT/GD) with AKTi and blue depicts downregulated pathways). *<0.05, **<0.01, ***<0.001, ****<0.0001.

The importance of PTEN phosphatase activity to suppress AKT signaling during organoid development is shown by the fact that AKT inhibition is sufficient to partially correct the morphological disruption induced by the *PTEN*^{G132D} allele. Organoids with the *PTEN*^{G132D} mutant allele failed to undergo epithelial mesenchymal transition (EMT), an essential process for neuroectoderm development. Although the AKT inhibitor failed to restore EMT, E-CDH and N-CDH expression shift, observed in organoids possessing the *PTEN*^{G132D} allele, we observed that AKT inhibition induced the upregulation of molecular pathways that drives neuronal fate. Moreover, these data show reduced lipid phosphatase activity of ASD-associated *PTEN*$^{G132D/WT}$ resulted in the most significant cellular disorganization and delayed differentiation of neuroectoderm compared to the cancer-associated *PTEN*$^{M134R/WT}$ mutant which activates AKT to lesser extents.

Upon forebrain induction, *PTEN*$^{WT/WT}$ and *PTEN*$^{M134R/WT}$ organoids down-modulated E-CDH expression and shifted to neuroepithelium fate with elevated N-CDH expression. However, *PTEN*$^{G132D/WT}$ organoids retained high levels of E-CDH expression and other stem cell markers. This failure to orchestrate the cadherin shift in early neurodevelopment are in line with recent studies that show convergent phenotypes in different ASD risk loci regarding asynchronous differentiation of neuron populations [61, 62]. Additionally, *PTEN* knockout forebrain organoid models have shown a delay in neuronal differentiation and an expansion of the proliferative pool of cells, which appears to be a common hallmark in genetic ASD pathology [63]. However, in this study we show that this phenomenon can occur in the early stages of neurodevelopment as neuroectoderm stem cell commitment. Our current findings inform the scientific community that the convergent pathological mechanism of genetic ASD may be partially dependent on the particular genetic perturbation within a given gene, and these mutations effect the development of the CNS.

As discussed above, we believe that the observed abnormalities in early FB development resulting from the *PTEN*^{G132D} mutation significantly impacts the phosphatase activity of PTEN leading to increase in AKT activation and increased levels of pGSK3β (Fig. 4d, e). Previous studies of GSK3β have shown that upon *PTEN* deletion, aberrantly activated AKT, which in turn, phosphorylates and suppresses GSK3β causing enhanced pluripotency maintenance, and negatively impacts the differentiation of mouse embryonic stem cells [60]. These data are interesting, since suppression of GSK3β via phosphorylation leads to increased β-catenin signaling that should drive cellular migration, and promote neuroectoderm formation [64, 65].

In our transcriptomic analysis, we also detected an upregulation of the ID1 and ID3 pathways. These DNA-binding protein inhibitors exert a role as repressors of neuronal differentiation [66]. We believe that these two molecules are playing a role in the observed differences between the *PTEN*$^{G132D/WT}$ and the *PTEN*$^{M132R/WT}$ genotypes, but we are still interrogating this possibility.

PTEN intricately interacts with multiple signaling networks, which perhaps explains the limited effect of AKT inhibition in our organoid study. For example, AKT inhibitor treatment of *PTEN*$^{G132D/WT}$ mutant organoids could not correct the continued expression of a stem cell-marker (E-CDH) during FB organoid induction, nor the unorganized cellular localization in the corticogenesis units or SVZ-like regions. PTEN hydrolyzes phosphatidylinositol-3,4,5-trisphosphate (PIP3) to phosphatidylinositol-,4,5-bisphosphate (PIP2) and PIP3 activate PDK1 kinase which phosphorylates and activates AKT. Over-activated PDK1 kinase in the absence of PTEN is reported to disrupt mouse neural plate development independently of downstream kinases, AKT or mTORC1 [50]. The substrate and the product of PTEN, i.e. PIP3 and PIP2, also regulate cytoskeleton activity, cellular polarity and motility [67–69]. In addition to its lipid phosphatase activity, PTEN has multiple functions in the nucleus, which is usually referred to as “non-canonical functions” [70]. Further studies to investigate these aspects regulated by *PTEN* are required for better understanding of pathogenesis of ASD caused by *PTEN* germline mutation.

Another unexplored avenue of our study is the characterization of *PTEN*$^{G132D/WT}$ and *PTEN*$^{M134R/WT}$ organoids past ~70 days. We sustained our organoid cultures for ~70 days, however, recent reports have indicated that forebrain organoid cultures can be sustained for up to 6 months to more accurately represent the heterogeneous cellular populations [71]. Examination of both *PTEN*-mutant organoids at advanced time points in neurodevelopment represents an important and necessary avenue to our future studies. In addition, gliogenesis, which is also affected in ASD, can be studied in long-term cultured brain organoids [72]. This would allow us to determine if there are sustained deficits to radial glial scaffolding, developmental deficits in astrocytes, and also permit the opportunity to determine if sustained AKTi or transient AKTi can rescue long-term deficits related to cellular migration and neuroectoderm development. Furthermore, later phase organoids would allow us the opportunity study electrophysiological changes in mature *PTEN*$^{G132D/WT}$ and *PTEN*$^{M134R/WT}$ organoids, and whether or not AKTi can possibly curtail deficits in neuronal function related to behaviors associated with ASD. These future experiments can be further enriched via the addition of microglia into our organoid culture systems. We have

previously demonstrated that *PTEN* dysfunction results in microglia dysfunction in the form of increased phagocytosis, synaptic stripping, and increased expression of pro-inflammatory genes [73, 74]. However, the mechanistic cause of the microgliosis remains unclear, and whether or not the microglial pathogenesis manifests itself as cell-autonomous, or as an exogenous pathology remains unclear due to the germline nature of the models used [73, 74]. The addition of healthy microglia may correct or even alleviate some of the deficits observed in $PTEN^{G132D/WT}$ and $PTEN^{M134R/WT}$ organoid neurodevelopment as others have previously shown that microglia are essential in expressing a wide variety of neurotrophic signaling molecules required for neuronal maturation and development [75].

The $PTEN^{G132D/WT}$ and $PTEN^{M134R/WT}$ organoids represent only a fraction of reported germline mutations observed in PHTS individuals, and represent 2 of many vastly understudied *PTEN* mutations [76]. Organoids can serve as an excellent in vitro system in trying to understand cellular and molecular mechanisms underlying the pathology of rare genetic germline disorders. The findings described above suggest that organoid models recapitulate some of the clinical phenotypes observed in our patients, making them a valuable tool for individualized phenotype prediction in the context of pathogenic germline *PTEN* mutations and other highly pleiotropic genetic conditions. Moreover, we hope that further generation and characterization of organoids containing clinically relevant *PTEN* mutations will allow us to generate accurate predictions as to what the pathology may be for PHTS patients.

DATA AVAILABILITY

Raw count matrix used for scRNAseq analysis is available in Supplementary Table 7.

CODE AVAILABILITY

The present study applied previously published approaches, of which codes are shared on public repositories: Seurat (https://github.com/satijalab/seurat), Monocle3 (https://github.com/cole-trapnell-lab/monocle3).

REFERENCES

1. American Psychiatric Association Diagnostic and Statistical Manual of Mental Disorders, Fifth Edition (DSM-5). Arlington, VA: American Psychiatric Publishing; 2013.
2. Lewis MH, Bodfish JW. Repetitive behavior disorders in autism. Ment Retard Dev D R. 1998;4:80–9.
3. Bodfish JW, Symons FJ, Parker DE, Lewis MH. Varieties of repetitive behavior in autism: comparisons to mental retardation. J Autism Dev Disord. 2000;30:237–43.
4. Mahoney WJ. The aggressive and impulsive child: Innovations in assessment and treatment - a commentary. Paediatr Child Health. 2004;9:537–8.
5. Esbensen AJ, Seltzer MM, Lam KS, Bodfish JW. Age-related differences in restricted repetitive behaviors in autism spectrum disorders. J Autism Dev Disord. 2009;39:57–66.
6. Minshew NJ, Williams DL. The new neurobiology of autism: cortex, connectivity, and neuronal organization. Arch Neurol. 2007;64:945–50.
7. Tilot AK, Frazier TW 2nd, Eng C. Balancing proliferation and connectivity in PTEN-associated autism spectrum disorder. Neurotherapeutics. 2015;12:609–19.
8. Fetit R, Hillary RF, Price DJ, Lawrie SM. The neuropathology of autism: a systematic review of post-mortem studies of autism and related disorders. Neurosci Biobehav R. 2021;129:35–62.
9. Paulsen B, Velasco S, Kedaigle A, Pigoni M, Quadrato G, Deo A. et al. Human brain organoids reveal accelerated development of cortical neuron classes as a shared feature of autism risk genes. Preprint at *bioRxiv* https://doi.org/10.1101/2020.11.10.376509 2020.
10. Zeidan-Chulia F, Salmina AB, Malinovskaya NA, Noda M, Verkhratsky A, Moreira JC. The glial perspective of autism spectrum disorders. Neurosci Biobehav Rev. 2014;38:160–72.
11. Tan MH, Mester JL, Ngeow J, Rybicki LA, Orloff MS, Eng C. Lifetime cancer risks in individuals with germline PTEN mutations. Clin Cancer Res. 2012;18:400–7.
12. Buxbaum JD, Cai G, Chaste P, Nygren G, Goldsmith J, Reichert J, et al. Mutation screening of the PTEN gene in patients with autism spectrum disorders and macrocephaly. Am J Med Genet B Neuropsychiatr Genet. 2007;144B:484–91.
13. Butler MG, Dasouki MJ, Zhou XP, Talebizadeh Z, Brown M, Takahashi TN, et al. Subset of individuals with autism spectrum disorders and extreme macrocephaly associated with germline PTEN tumour suppressor gene mutations. J Med Genet. 2005;42:318–21.
14. McBride KL, Varga EA, Pastore MT, Prior TW, Manickam K, Atkin JF, et al. Confirmation study of PTEN mutations among individuals with autism or developmental delays/mental retardation and macrocephaly. Autism Res. 2010;3:137–41.
15. Varga V, Losonczy A, Zemelman BV, Borhegyi Z, Nyiri G, Domonkos A, et al. Fast synaptic subcortical control of hippocampal circuits. Science. 2009;326:449–53.
16. O'Roak BJ, Vives L, Fu W, Egertson JD, Stanaway IB, Phelps IG, et al. Multiplex targeted sequencing identifies recurrently mutated genes in autism spectrum disorders. Science. 2012;338:1619–22.
17. Fu JM, Satterstrom FK, Peng M, Brand H, Collins RL, Dong S, et al. Rare coding variation provides insight into the genetic architecture and phenotypic context of autism. Nat Genet. 2022;54:1320–31.
18. Simons Fundation Autism Research Initiative (SFARI). 2023. https://gene.sfari.org/database/human-gene/
19. Lee H, Thacker S, Sarn N, Dutta R, Eng C. Constitutional mislocalization of Pten drives precocious maturation in oligodendrocytes and aberrant myelination in model of autism spectrum disorder. Transl Psychiatry. 2019;9:13.
20. Kathuria A, Lopez-Lengowski K, Jagtap SS, McPhie D, Perlis RH, Cohen BM, et al. Transcriptomic landscape and functional characterization of induced pluripotent stem cell-derived cerebral organoids in schizophrenia. JAMA Psychiatry. 2020;77:745–54.
21. Shou Y, Liang F, Xu S, Li X. The application of brain organoids: from neuronal development to neurological diseases. Front Cell Dev Biol. 2020;8:579659.
22. Lancaster MA, Knoblich JA. Generation of cerebral organoids from human pluripotent stem cells. Nat Protoc. 2014;9:2329–40.
23. Bershteyn M, Nowakowski TJ, Pollen AA, Di Lullo E, Nene A, Wynshaw-Boris A, et al. Human iPSC-derived cerebral organoids model cellular features of lissencephaly and reveal prolonged mitosis of outer radial glia. Cell Stem Cell. 2017;20:435–49.e4.
24. Di Lullo E, Kriegstein AR. The use of brain organoids to investigate neural development and disease. Nat Rev Neurosci. 2017;18:573–84.
25. Lancaster MA, Renner M, Martin CA, Wenzel D, Bicknell LS, Hurles ME, et al. Cerebral organoids model human brain development and microcephaly. Nature. 2013;501:373–9.
26. Tiscornia G, Vivas EL, Izpisua, Belmonte JC. Diseases in a dish: modeling human genetic disorders using induced pluripotent cells. Nat Med. 2011;17:1570–6.
27. Soldner F, Jaenisch R. Medicine. iPSC disease modeling. Science. 2012;338:1155–6.
28. Bock DD, Lee WC, Kerlin AM, Andermann ML, Hood G, Wetzel AW, et al. Network anatomy and in vivo physiology of visual cortical neurons. Nature. 2011;471:177–82.
29. Kim DS, Ross PJ, Zaslavsky K, Ellis J. Optimizing neuronal differentiation from induced pluripotent stem cells to model ASD. Front Cell Neurosci. 2014;8:109.
30. Qian X, Nguyen HN, Song MM, Hadiono C, Ogden SC, Hammack C, et al. Brain-region-specific organoids using mini-bioreactors for modeling ZIKV exposure. Cell. 2016;165:1238–54.
31. Qian X, Jacob F, Song MM, Nguyen HN, Song H, Ming GL. Generation of human brain region-specific organoids using a miniaturized spinning bioreactor. Nat Protoc. 2018;13:565–80.
32. Adhya D, Swarup V, Nagy R, Dutan L, Shum C, Valencia-Alarcon EP, et al. Atypical neurogenesis in induced pluripotent stem cells from autistic individuals. Biol Psychiatry. 2021;89:486–96.
33. Chan WK, Griffiths R, Price DJ, Mason JO. Cerebral organoids as tools to identify the developmental roots of autism. Mol Autism. 2020;11:58.
34. Leslie NR, Batty IH, Maccario H, Davidson L, Downes CP. Understanding PTEN regulation: PIP2, polarity and protein stability. Oncogene. 2008;27:5464–76.
35. Sanchez-Alegria K, Flores-Leon M, Avila-Munoz E, Rodriguez-Corona N, Arias C. PI3K signaling in neurons: a central node for the control of multiple functions. Int J Mol Sci. 2018;19:3725.
36. Vanderplow AM, Eagle AL, Kermath BA, Bjornson KJ, Robison AJ, Cahill ME. Akt-mTOR hypoactivity in bipolar disorder gives rise to cognitive impairments associated with altered neuronal structure and function. Neuron. 2021;109:1479–96.e1476.
37. Chen YH, Pruett-Miller SM. Improving single-cell cloning workflow for gene editing in human pluripotent stem cells. Stem Cell Res. 2018;31:186–92.
38. Hitomi M, Stacey DW. The checkpoint kinase ATM protects against stress-induced elevation of cyclin D1 and potential cell death in neurons. Cytom A. 2010;77:524–33.
39. Kang SC, Jaini R, Hitomi M, Lee H, Sarn N, Thacker S, et al. Decreased nuclear Pten in neural stem cells contributes to deficits in neuronal maturation. Mol Autism. 2020;11:43.
40. Hao Y, Hao S, Andersen-Nissen E, Mauck WM, Zheng S, Butler A, et al. Integrated analysis of multimodal single-cell data. Cell. 2021;184:3573–87.e29.
41. Cao J, Spielmann M, Qiu X, Huang X, Ibrahim DM, Hill AJ, et al. The single-cell transcriptional landscape of mammalian organogenesis. Nature. 2019;566:496–502.

42. Qiu X, Mao Q, Tang Y, Wang L, Chawla R, Pliner HA, et al. Reversed graph embedding resolves complex single-cell trajectories. Nat Methods. 2017;14:979–82.
43. Trapnell C, Cacchiarelli D, Grimsby J, Pokharel P, Li S, Morse M, et al. The dynamics and regulators of cell fate decisions are revealed by pseudotemporal ordering of single cells. Nat Biotechnol. 2014;32:381–6.
44. Howard BM, Zhicheng M, Filipovic R, Moore AR, Antic SD, Zecevic N. Radial glia cells in the developing human brain. Neuroscientist. 2008;14:459–73.
45. Lopez-Tobon A, Villa CE, Cheroni C, Trattaro S, Caporale N, Conforti P, et al. Human cortical organoids expose a differential function of GSK3 on cortical neurogenesis. Stem Cell Rep. 2019;13:847–61.
46. Kalebic N, Gilardi C, Stepien B, Wilsch-Brauninger M, Long KR, Namba T, et al. Neocortical expansion due to increased proliferation of basal progenitors is linked to changes in their morphology. Cell Stem Cell. 2019;24:535-50.
47. Tischfield MA, Baris HN, Wu C, Rudolph G, Van Maldergem L, He W, et al. Human TUBB3 mutations perturb microtubule dynamics, kinesin interactions, and axon guidance. Cell. 2010;140:74–87.
48. Lui JH, Hansen DV, Kriegstein AR. Development and evolution of the human neocortex. Cell. 2011;146:18–36.
49. Beattie R, Hippenmeyer S. Mechanisms of radial glia progenitor cell lineage progression. FEBS Lett. 2017;591:3993–4008.
50. Grego-Bessa J, Bloomekatz J, Castel P, Omelchenko T, Baselga J, Anderson KV. The tumor suppressor PTEN and the PDK1 kinase regulate formation of the columnar neural epithelium. eLife. 2016;5:e12034.
51. Hribkova H, Grabiec M, Klemova D, Slaninova I, Sun YM. Calcium signaling mediates five types of cell morphological changes to form neural rosettes. J Cell Sci. 2018;131:jcs206896.
52. Shen WH, Balajee AS, Wang J, Wu H, Eng C, Pandolfi PP, et al. Essential role for nuclear PTEN in maintaining chromosomal integrity. Cell. 2007;128:157–70.
53. Paez J, Sellers WR. PI3K/PTEN/AKT pathway. A critical mediator of oncogenic signaling. Cancer Treat Res. 2003;115:145–67.
54. He X, Saji M, Radhakrishnan D, Romigh T, Ngeow J, Yu Q, et al. PTEN lipid phosphatase activity and proper subcellular localization are necessary and sufficient for down-regulating AKT phosphorylation in the nucleus in Cowden syndrome. J Clin Endocrinol Metab. 2012;97:E2179–2187.
55. Fournier MV, Fata JE, Martin KJ, Yaswen P, Bissell MJ. Interaction of E-cadherin and PTEN regulates morphogenesis and growth arrest in human mammary epithelial cells. Cancer Res. 2009;69:4545–52.
56. Mighell TL, Thacker S, Fombonne E, Eng C, O'Roak BJ. An integrated deep-mutational-scanning approach provides clinical insights on PTEN genotype-phenotype relationships. Am J Hum Genet. 2020;106:818–29.
57. Matreyek KA, Stephany JJ, Ahler E, Fowler DM. Integrating thousands of PTEN variant activity and abundance measurements reveals variant subgroups and new dominant negatives in cancers. Genome Med. 2021;13:165.
58. Larue L, Ohsugi M, Hirchenhain J, Kemler R. E-cadherin null mutant embryos fail to form a trophectoderm epithelium. Proc Natl Acad Sci USA. 1994;91:8263–7.
59. Di Cristofano A, Pesce B, Cordon-Cardo C, Pandolfi PP. Pten is essential for embryonic development and tumour suppression. Nat Genet. 1998;19:348–55.
60. Wang W, Lu G, Su X, Tang C, Li H, Xiong Z, et al. Pten-mediated Gsk3beta modulates the naive pluripotency maintenance in embryonic stem cells. Cell Death Dis. 2020;11:107.
61. Paulsen B, Velasco S, Kedaigle AJ, Pigoni M, Quadrato G, Deo AJ, et al. Autism genes converge on asynchronous development of shared neuron classes. Nature. 2022;602:268–73.
62. Sullivan JM, De Rubeis S, Schaefer A. Convergence of spectrums: neuronal gene network states in autism spectrum disorder. Curr Opin Neurobiol. 2019;59:102–11.
63. Li Y, Muffat J, Omer A, Bosch I, Lancaster MA, Sur M, et al. Induction of expansion and folding in human cerebral organoids. Cell Stem Cell. 2017;20:385–396.e3.
64. Hermida MA, Dinesh Kumar J, Leslie NR. GSK3 and its interactions with the PI3K/AKT/mTOR signalling network. Adv Biol Regul. 2017;65:5–15.
65. Leung AW, Murdoch B, Salem AF, Prasad MS, Gomez GA, Garcia-Castro MI. WNT/beta-catenin signaling mediates human neural crest induction via a pre-neural border intermediate. Development. 2016;143:398–410.
66. Zhang G, Lübke L, Chen F, Beil T, Takamiya M, Diotel N, et al. Neuron-radial glial cell communication via BMP/Id1 signaling is key to long-term maintenance of the regenerative capacity of the adult zebrafish telencephalon. Cells. 2021;10:2794.
67. Insall RH, Weiner OD. PIP3, PIP2, and cell movement-similar messages, different meanings? Dev Cell. 2001;1:743–7.
68. Thapa N, Anderson RA. PIP2 signaling, an integrator of cell polarity and vesicle trafficking in directionally migrating cells. Cell Adh Migr. 2012;6:409–12.
69. Wu H, Feng W, Chen J, Chan LN, Huang SY, Zhang MJ. PDZ domains of Par-3 as potential phosphoinositide signaling integrators. Mol Cell. 2007;28:886–98.
70. Planchon SM, Waite KA, Eng C. The nuclear affairs of PTEN. J Cell Sci. 2008;121:249–53.
71. Giandomenico SL, Sutcliffe M, Lancaster MA. Generation and long-term culture of advanced cerebral organoids for studying later stages of neural development. Nat Protoc. 2021;16:579–602.
72. Qian X, Su Y, Adam CD, Deutschmann AU, Pather SR, Goldberg EM, et al. Sliced human cortical organoids for modeling distinct cortical layer formation. Cell Stem Cell. 2020;26:766–81.e769.
73. Sarn N, Thacker S, Lee H, Eng C. Germline nuclear-predominant Pten murine model exhibits impaired social and perseverative behavior, microglial activation, and increased oxytocinergic activity. Mol Autism. 2021;12:41.
74. Sarn N, Jaini R, Thacker S, Lee H, Dutta R, Eng C. Cytoplasmic-predominant Pten increases microglial activation and synaptic pruning in a murine model with autism-like phenotype. Mol Psychiatry. 2021;26:1458–71.
75. Poyhonen S, Er S, Domanskyi A, Airavaara M. Effects of neurotrophic factors in glial cells in the central nervous system: expression and properties in neurodegeneration and injury. Front Physiol. 2019;10:486.
76. Yehia L, Keel E, Eng C. The clinical spectrum of PTEN mutations. Annu Rev Med. 2020;71:103–16.

ACKNOWLEDGEMENTS

This work was funded in part by the Ambrose Monell PTEN Switch grant (to CE) and the Lisa Dean Mosley Foundation (to CE and MH). JV is an Ambrose Monell Cancer Genomic Medicine Fellow (to CE). CE is the Sondra J. and Stephen R. Hardis Endowed Chair of Cancer Genomic Medicine at the Cleveland Clinic and is an ACS Clinical Research Professor.

AUTHOR CONTRIBUTIONS

SK, MH, ZT performed experiments and data analysis. SK, MH, CE designed experiments, NS, SK, JV wrote the manuscript, JV conducted the transcriptomic analysis, and CE oversaw and manage project design and progress until completion.

COMPETING INTERESTS

The authors declare no competing interests.

ADDITIONAL INFORMATION

Supplementary information The online version contains supplementary material available at https://doi.org/10.1038/s41380-023-02325-3.

Correspondence and requests for materials should be addressed to Charis Eng.